Computer Modeling in Engineering & Sciences

Tech Science Press

https://doi.org/10.32604/cmes.2026.082801

ARTICLE

Influence of Autonomous Vehicle Front-End Geometry on Pedestrian Injury Redistribution: A Multibody Simulation Study

Adrian Soica and Bogdan Cornel Benea*

Department of Automotive and Transport Engineering, Transilvania University of Brasov, Brasov, Romania

*Corresponding Author: Bogdan Cornel Benea. Email: b.benea@unitbv.ro

Received: 23 March 2026; Accepted: 27 May 2026; Published: 30 June 2026

ABSTRACT: This study investigates the influence of autonomous vehicle (AV) front-end geometry on pedestrian injury biomechanics using PC-Crash multibody simulations. While emerging vehicles promise improved urban safety through automation and collision avoidance technologies, their unconventional front-end architectures introduce new passive safety challenges. The research compares classical passenger vehicles with van-type and symmetric flat-front autonomous platforms under standardized impact conditions at 40 km/h. Results reveal a clear redistribution of injury mechanisms depending on vehicle geometry. Conventional sloped front-end vehicles, super-mini and compact class, generate higher Head Injury Criterion (HIC) values due to wrap-around kinematics, where pedestrians rotate onto the hood and windshield. In contrast, vertically oriented and flat-front autonomous designs significantly reduce HIC values by suppressing rotational motion. However, this reduction in head injury risk is accompanied by substantially increased thoracic peak forces, particularly in ROBO1-type configurations, where chest loads exceeded 15 kN. The findings demonstrate that lower HIC values do not necessarily indicate improved overall pedestrian safety. Instead, emerging autonomous geometries shift injury risk from the head to the thorax and lower limbs. The study highlights the need for balanced multi-criteria pedestrian assessment frameworks that incorporate thoracic injury metrics, geometric optimization, and stiffness distribution considerations in early-stage autonomous vehicle design.

KEYWORDS: Autonomous vehicles; pedestrian impact; accident reconstruction; collision type

1 Introduction

Pedestrian–vehicle accidents occur predominantly in urban environments, where interactions between vehicles and vulnerable road users are frequent. Statistical data indicate that approximately 80%–85% of pedestrian fatalities and serious injuries take place in urban areas, highlighting the increased risk associated with dense traffic, mixed road use, and complex infrastructure [1]. Globally, similar trends are observed, with urban settings accounting for the majority of pedestrian casualties, emphasizing the need for improved vehicle design and urban safety measures [2].

The advent of autonomous vehicle (AV) services represents a transformative shift in urban transportation and city design. These self-driving vehicles leverage advanced sensor suites, artificial intelligence, and real-time data to navigate complex urban environments without human drivers, offering the promise of safer, more efficient, and more sustainable mobility systems. By optimizing traffic flow and minimizing human error, autonomous vehicles have the potential to significantly improve road safety; human error accounts for the vast majority of traffic accidents in conventional driving contexts, and automation could markedly reduce this source of risk [3]. Enhanced efficiency in urban traffic could also free up valuable road space and

reduce the need for expansive parking infrastructure; studies suggest that AV could reduce parking demand by up to 90% in dense urban cores, enabling the reallocation of space to pedestrians, green areas, and mixed-use developments [4]. Moreover, by facilitating shared mobility services, emerging vehicle can complement public transportation systems, improving first-mile/last-mile connectivity and accessibility, particularly for elderly or mobility-impaired populations [5].

Despite these opportunities, the integration of AT into existing urban architecture is not without substantial challenges. Current infrastructure, including roadways, traffic signaling, and communication network is predominantly designed for human drivers and may require significant upgrades to support autonomous operations securely and reliably. Smart infrastructure capable of real-time communication with AV is essential to fully realize efficiency gains and safety outcomes. Beyond efficiency and automation, pedestrian safety emerges as a central concern and opportunity in this transition. Urban areas concentrate vulnerable road users, pedestrians, cyclists, and micromobility users, who account for a disproportionate share of traffic-related injuries and fatalities. AT or shared autonomous vehicles (SAV), if properly designed and integrated, have the potential to significantly reduce these risks.

The advantage of AV lies in their ability to reduce crashes caused by human error, which remains the dominant factor in vehicle–pedestrian collisions. Autonomous driving systems employ continuous environmental perception using cameras, radar, and LiDAR to detect pedestrians and anticipate their movements. These capabilities enable automated emergency braking and trajectory adjustments that can significantly reduce impact speeds or avoid collisions altogether [6]. Since pedestrian injury severity, particularly head and thoracic trauma, is strongly correlated with vehicle speed at impact, even modest speed reductions can yield substantial safety benefits [7]. Overall, the successful integration of autonomous vehicles and taxis into urban architecture depends on a holistic approach that combines advanced vehicle technology, pedestrian-oriented vehicle design, supportive infrastructure, and robust regulatory oversight, with pedestrian safety as a central design criterion.

The design of AT front ends, Fig. 1, influences not only crash avoidance capabilities but also the severity of pedestrian injuries when collisions occur. Unlike traditional vehicles, these integrate advanced sensor suites and active safety systems like pedestrian detection and automated emergency braking, that work with geometric design to reduce impact risk and severity. Vehicle front-end geometry directly governs pedestrian kinematics immediately after impact. Key parameters such as bumper height, hood leading edge height, and front-end inclination determine whether the pedestrian undergoes wrap-around motion or direct forward projection. These mechanisms strongly influence load transfer to the head, thorax, and lower extremities.

Recent safety data from operational robotaxi fleets indicate that autonomous vehicles can achieve substantially fewer pedestrian injuries compared to human-driven cars, as evidenced by studies showing up to a 92% reduction in pedestrian injuries and reduced crash incidence after millions of miles of autonomous driving, although more data are required to draw definitive conclusions about serious injury prevention [8]. However, real-world incidents involving autonomous vehicle demonstrate that pedestrian collisions still occur and can lead to injury, highlighting that current perception and control systems—and the physical design of the front structure—must be optimized to complement software safety systems. Researchers argue that soft, compliant front structures, integrated with emerging vehicle perception and braking systems, will be critical in reducing injury severity should a collision become unavoidable [9]. In parallel, studies underscore that pedestrian perception of autonomous vehicles, including how vehicle size, yielding behaviour, and external signalling affect pedestrian decision-making—should inform both front-end design and human-machine interaction strategies to enhance safety and trust in automated urban environments [10]. New design concepts are proposed both to increase user confidence in AV and to facilitate access for people with disabilities. Large glass spaces, easy access paths with a ground clearance lowered to sidewalk level.

Some design principles were adopted to optimize the experience with SAV. The anthropomorphic design emphasizes incorporating human-like traits into the vehicle to strengthen emotional connections with users. Defensible space ensures clear boundaries and territoriality, allowing passengers to feel a sense of control over their environment. The transparency system focuses on keeping users informed about the SAV's status and journey, enhancing trust and clarity. Personalization features enable a tailored experience by offering customizable options that meet the specific needs of individual passengers. Finally, creating a restorative environment through design fosters relaxation and positive emotions, promoting well-being during the ride. These principles work together to ensure that the SAV experience is intuitive, comforting, and user-centered [11]. A good part of these design concepts is reflected in external passive safety, through contact between vehicles and vulnerable road users.

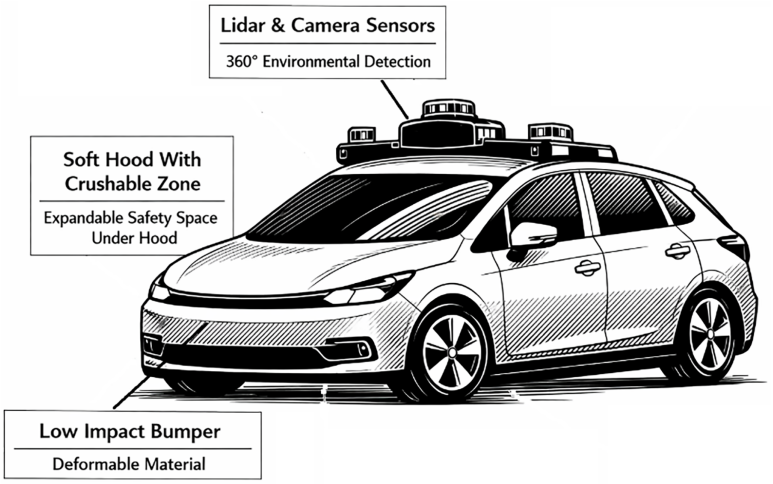

Figure 1: Autonomous vehicle design.

Analysis of the pedestrian crash database in the United States indicates that injuries to the lower extremities and the head are the most common outcomes in vehicle–pedestrian collisions, with head injuries generally representing the most severe trauma [12] (Chidester and Isenberg, 2001). Moreover, injury source analysis reveals notable differences in head impact locations depending on vehicle type. In SUV-related collisions, the bonnet (hood) is identified as the primary contributor to head injuries, whereas in passenger car impacts, the windscreen constitutes the dominant source of head trauma [13] (Longhitano et al., 2005). Pedestrians struck by sport utility vehicles have approximately twice the risk of sustaining traumatic brain injuries compared with those impacted by passenger cars [14] (Ballesteros et al., 2004).

2 Research Gaps in Literature and Motivation

While general trends linking bumper height, hood leading edge height, and front-end stiffness to pedestrian injury severity are known, quantitative relationships between specific geometric parameters and biomechanical injury metrics remain insufficiently defined. In particular, the combined effects of front-end height, curvature, and stiffness distribution on pedestrian kinematics and injury outcomes require further investigation. Passive safety research has traditionally focused on primary vehicle–pedestrian contact. However, secondary impacts such as pedestrian contact with the ground or other roadside elements can contribute significantly to overall injury severity. Previous studies have clearly demonstrated that vehicle front-end geometry plays a decisive role not only in the primary impact but also in shaping the mechanism of secondary pedestrian-ground contact. For instance, Gupta and Yang [15] showed that variations in

bumper height, bonnet leading-edge height, and hood geometry can significantly influence pedestrian kinematics, leading in most cases to head/neck/shoulder ground impact, but also, for certain geometries, to configurations where lower extremities contact the ground first, thereby reducing the risk of secondary head impact. Furthermore, their results indicate that even active safety solutions such as pop-up hoods, while effective in reducing head injury during the primary vehicle contact, may alter pedestrian kinematics in a way that does not prevent and may even worsen the severity of the secondary ground impact. This highlights the complex and sometimes counterintuitive relationship between vehicle design and overall injury outcome.

Similarly, multibody simulation studies have shown that vehicle front-end geometry strongly affects post-impact pedestrian kinematics, including rotation, launch conditions, and flight trajectory. In particular, parameters such as bonnet leading-edge height and hood angle significantly influence the likelihood of head-first ground impact, as well as the severity of the secondary impact [16]. These findings confirm that pedestrian injury mechanisms are governed by the combined effects of vehicle geometry and kinematic evolution after impact.

Although regulatory testing has improved minimum safety performance, there is a lack of clear, design-oriented guidelines that translate pedestrian injury biomechanics into practical front-end geometry and material solutions. This gap limits the proactive integration of pedestrian safety considerations early in vehicle design.

Pedestrian injury assessment in vehicle impacts is traditionally based on biomechanical criteria derived from standardized experimental procedures, such as the Head Injury Criterion (HIC), which evaluates the time-integrated resultant head acceleration and is widely adopted in regulations and consumer testing protocols (e.g., EuroNCAP, ISO TS 13499). However, these criteria and associated test procedures have been primarily developed for conventional passenger vehicle geometries characterized by sloped front-end profiles. This creates a fundamental limitation when assessing emerging autonomous vehicle architectures, which often feature higher, flatter, or vertically oriented front-end designs. In such configurations, the pedestrian kinematics and load transfer mechanisms differ significantly, potentially leading to a redistribution of injury risk across different body regions.

The main research gap addressed in this study is therefore the lack of a design-oriented understanding of how front-end geometry influences the redistribution of pedestrian injury mechanisms beyond head-focused criteria. In particular, current assessment frameworks do not explicitly account for the trade-off between reduced head injury risk and increased thoracic loading observed in non-conventional vehicle geometries.

The novelty of this work lies in demonstrating, through controlled multibody simulations, that autonomous vehicle front-end geometry does not uniformly reduce injury severity, but instead redistributes it spatially and temporally, highlighting the need for multi-criteria pedestrian safety evaluation approaches.

In this paper, using the PC-Crash 15.1 software, we aimed to analyze the forces that occur at the contact between the vehicle and the pedestrian, to determine the head injury criterion, and to evaluate the forces generated during contact with the ground. PC-Crash is an application widely used by specialists in traffic accident analysis and reconstruction, whose models have been validated in numerous published studies, among which references [17]—pedestrian in contact with vehicle phase, [18]—pedestrian impact, [19]—PC-Crash validation of pedestrian model, [20]—PC-Crash validation Sport Bike Motorcycle model and [21]—improvement of the reconstruction process using the variation factors such the pedestrian height, collision angle, hood height and pedestrian-road friction coefficient, [22]—pedestrian throw distance, [23]—a review of pedestrian impact simulation, can be cited. Also, PC-Crash is a widely used tool in accident reconstruction and pedestrian impact analysis, whose multibody models have been

validated in numerous studies against experimental data, including cadaver tests, dummy experiments, and real-world accident reconstructions. The pedestrian is represented as a multibody system composed of interconnected rigid segments, with motion governed by Newton–Euler equations and contact forces modeled using stiffness-based formulations [24].

3 Consideration upon Vehicle Front End Geometry and Models

Vehicle front-end geometry has been widely recognized as an important factor influencing pedestrian injury mechanisms and severity during vehicle–pedestrian collisions [25]. Early research established that the geometric relationship between the bumper, hood leading edge, and windshield governs pedestrian kinematics immediately after impact, determining whether the pedestrian is rotated onto the hood or struck directly at the torso or head level [26] (Niederer & Schlumpf, 1984).

More recent accident reconstruction studies confirm that vehicles with higher and more vertical front-end profiles, commonly associated with sport utility vehicles, vans, and pickup trucks, present a significantly increased risk of severe and fatal pedestrian injuries. Hu et al. (2024) [27] demonstrated that tall, blunt front ends are associated with substantially higher pedestrian fatality risk compared to low, sloped designs, largely due to higher impact points on the body and unfavorable post-impact kinematics. Similarly, Monfort et al. (2024) [28] showed that increased hood leading edge height correlates strongly with severe pelvis, thorax, and head injuries.

In addition to primary impact effects, front-end geometry also influences ground impact severity. Higher front ends tend to project pedestrians forward, increasing head impact velocity with the ground. These findings emphasize that pedestrian protection cannot rely solely on material compliance but must also consider geometric optimization. Overall, the literature indicates that lower, more sloped front-end geometries, combined with energy-absorbing structures, offer improved pedestrian safety outcomes.

A typical bumper system consists of a curved beam support structure, shock-absorbing mounting elements, and an elastic fascia manufactured from hard thermoplastics such as polycarbonate, polyurethane, high-density polyethylene, polypropylene, or thermoplastic rubber. The bumper operates as part of a larger system that includes shock absorbers, frontal frames, radiator supports, and headlight protection. Recent studies indicate that adaptive bumpers using anisotropic materials may significantly enhance pedestrian friendliness while maintaining durability, although further mechanical development is required before full-scale implementation [29].

Elastic and high-strength bumper structures have an important role in reducing the effects of frontal and rear impacts by partially absorbing collision forces together with the vehicle side members. Most crash scenarios involving bumpers are classified as low-speed collisions, with bumpers primarily designed to limit damage at speeds below 16 kph, as reported in [30,31]. Over time, the protective role of the bumper cross-member has diminished in importance, as vehicle aesthetics and aerodynamic performance became higher priorities. However, research later highlighted that the stiffness and deformation behaviour of bumper structures and their supports are factors that improve pedestrian protection, as controlled deformation can reduce impact forces on pedestrians.

One of initial vehicle classification, proposed in [32], was developed based on DEKRA research conducted for the EEVC-WG17 working group. This identifies the six most common types of vehicle front-end profiles. This classification is intended to represent the typical geometrical configurations encountered in passenger vehicles. The main geometric characteristics associated with each frontal profile are summarized in the corresponding Table 1.

Table 1: Vehicle profile classification upon [32].

	Height of Bonnet Front Edge [m]	Bonnet Inclination Angle [°]	Angle Determined by the Bumper Upper Edge and the Bonnet Front Edge [°]
Key profile	<0.7	<20	
Trapezoidal profile			
Superficial bonnet inclination		<20	<70
Pronounced bonnet inclination		>20	<70
Ellipsoidal profile		Bonnet front edge has a radius of curvature > 0.25 m	
Pontoon profile			>70
Vertical profile (BOX)		Vertically contact plan	

In the paper, by using the PC-Crash software, the vehicle's frontal geometry parameters were modified, according to Fig. 2 and Table 2. By adjusting the parameters that define the front-end geometry, multiple vehicle profiles can be generated.

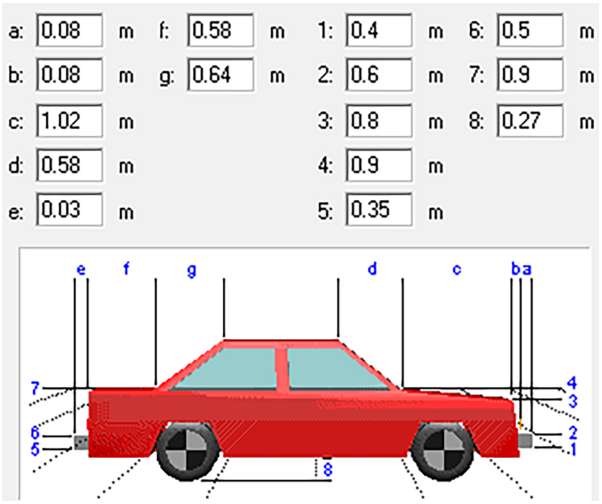

Figure 2: PC-Crash vehicle geometry setup.

Table 2: PC-Crash vehicle geometry setup.

No. Param	PC-Crash/Vehicle's Profile	Parameter Description
P1	1	Height of the bumper lower edge
P2	2	Height of the bumper upper edge
P3	3	Height of the bonnet front edge
P4	4	Height of the bonnet rear edge
P5	a	Bumper width (bumper advance)
P6	b	Front edge advance of bonnet
P7	c	Bonnet length
P8	d	Windshield length
P9	8	Ground clearance

Because vehicle geometry can significantly influence pedestrian kinematics during an impact, the simulation model allows the use of different vehicle shapes. The main characteristics of the vehicles considered in the simulations are presented in Table 3. Six types of vehicles from different size classes were chosen for the study. These models were chosen from the PC-Crash database, so as to simulate as well as possible the experimental vehicle shapes with which the major developers of autonomous vehicles conduct tests on public roads. In addition to the vehicles with "classic" geometric shapes from Super mini to VAN, two geometries that are not found in the PC-CRASH database, but which are in the current trend of autonomous vehicle design, were analyzed, Amazon Zoox [33], which it the most unconventional Minibus shape and another presented in [11], Fig. 3. For these two typologies, the geometry was generated from the PC-Crash interface, modifying the geometric parameters presented in Fig. 2 and Table 2.

Table 3: Vehicle characteristics and classification; source: PC-CRASH.

Vehicle Type	Mass [kg]	Height [m]	a [m]	b [m]	c [m]	d [m]	1 [m]	2 [m]	3 [m]	4 [m]
SM	795	1.465	0.050	0.058	0.871	0.498	0.350	0.500	0.837	0.942
CC	1395	1.462	0.050	0.067	1.167	0.667	0.350	0.500	0.835	0.940
SSUV	1585	1.700	0.050	0.065	1.130	0.646	0.340	0.550	0.971	1.093
EC	2135	1.480	0.050	0.076	1.335	0.763	0.350	0.520	0.846	0.951
VAN1	2001	2362	0.055	0.100	0.940	0.920	0.550	0.700	1.300	1.485
VAN2	1405	1.940	0.075	0.000	0.090	0.280	0.300	0.435	1.150	1.240
ROBO1	2650	1.936	0.000	0.050	0.050	0.150	0.350	0.500	1.106	1.245
ROBO2	1800	1.736	0.100	0.000	0.700	0.100	0.600	0.800	0.800	1.000

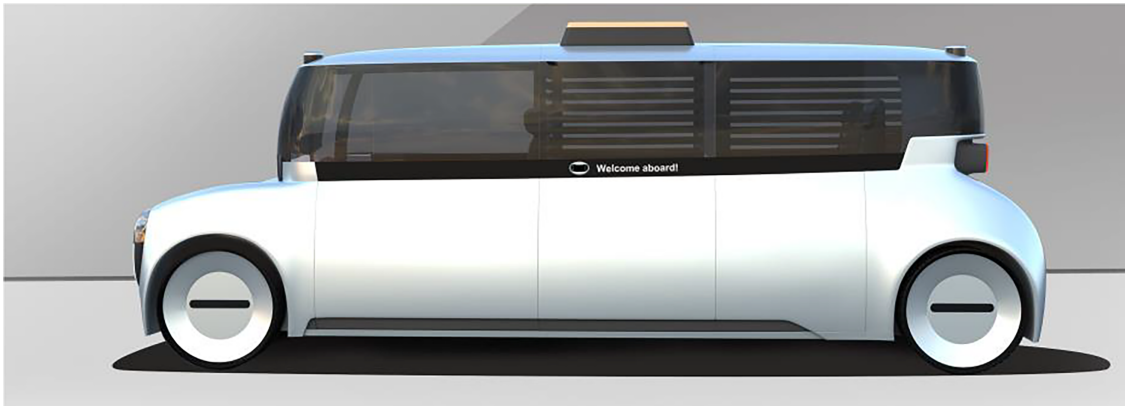

Figure 3: Autonomous vehicle concept, source [11].

Vehicle characteristics used in the simulations are derived from the validated PC-Crash database, which includes representative geometries and physical parameters for different vehicle classes (e.g., super-mini, compact, SUV, van). These predefined modes are based on experimentally informed dimensions and have been widely used in accident reconstruction studies. In addition, for emerging autonomous vehicle concepts not directly available in the database, such as flat-front or symmetric designs, the vehicle geometry was generated parametrically by modifying key front-end parameters, including bumper height, bonnet leading edge height, and front surface inclination. This parametric approach enables controlled investigation of the influence of geometry while maintaining a physically consistent modeling framework.

The selection of vehicle geometries was based on both representativeness and methodological coverage. Conventional vehicle classes (SM, CC, SSUV, EC, VAN) were selected from the validated PC-Crash database, ensuring realistic geometric representation. In addition, two non-conventional autonomous vehicle configurations were introduced to reflect emerging design trends characterized by flat or vertical front-end profiles.

Rather than representing specific commercial vehicles, the analyzed configurations should be interpreted as representative geometric archetypes spanning the full spectrum of front-end designs, from sloped passenger cars to vertical autonomous platforms. This approach enables a systematic investigation of the influence of geometry alone on pedestrian impact biomechanics.

The vehicles in PC-Crash are modeled as rigid bodies for multibody pedestrian contacts. The surface of the vehicle is defined by several planes, which are defined by triangular polygons. The vehicle shape can be specified either by entering specific geometrical distances to describe the vehicle shape or by using detailed 3D vehicle shapes imported as DXF drawings. The assumption is made that the point of contact is on the surface of the vehicle plane. Thus, vehicle deformation is neglected. The point of contact has to be inside the three points that define the vehicle's triangular polygonal plane being contacted. The penetration of the ellipsoid is the distance between a point on the ellipsoid where the tangential plane is parallel to the contacting plane, and the contacting plane. The tangential components of the contact force are calculated using the specified ellipsoid to vehicle friction coefficient and the relative velocity of the contact points. The contact force from the ellipsoid is applied as an external force to the vehicle. Therefore, the influence of a pedestrian impact on the vehicle's post-impact motion can be analyzed [34].

The vehicle is modeled as a rigid body composed of planar polygonal surfaces.

The contact relations, according to Fig. 4, are:

$$\mathrm{n}_e = -\mathrm{n}_p \tag{1}$$

$$\lambda = \left| \mathrm{P}_e - \mathrm{P}_p \right. \tag{2}$$

$$\mathrm{F}_{ne} = -\lambda S_e \mathrm{n}_e \tag{3}$$

$$\mathrm{F}_{np} = -\mathrm{F}_{ne} \tag{4}$$

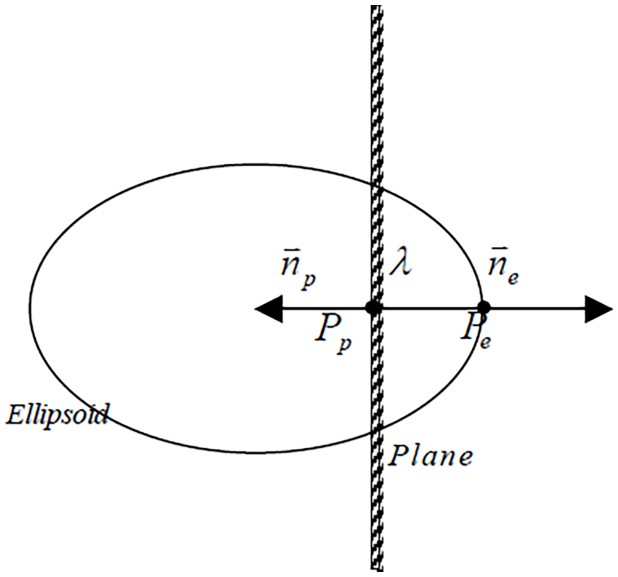

Figure 4: Vehicle pedestrian contact model [34].

Friction force can be expessed as:

$$\mathrm{F}_t = \left| \mathrm{F}_n \right| \cdot \mu \cdot \frac{\mathrm{v}_{rel}}{\left| \mathrm{v}_{rel} \right|} \tag{5}$$

where:

- n_e is normal vector at the contact point on the ellipsoid (pedestrian body segment)
- n_p is normal vector of the vehicle contact surface (polygon/plane)
- λ is the penetration depth,
- F_{np}, F_{ne} is normal contact force components onto ellipsoid and plane,
- F_{tp}, F_{te} is tangential contact force components onto ellipsoid and plane,
- S is the stiffness coefficient,
- μ is the friction coefficient,
- v_{rel} is the relative velocity at the contact point.

The vehicle geometry may be defined either by selecting a defined shape from the software menu, Fig. 2, or by importing a detailed three-dimensional DXF model and associating it with the vehicle [34]. The model applies a linear stiffness formulation with restitution to describe impact behavior [35]. Also, in PC-Crash, simplified 3D DXF vehicle models are employed for contact calculations. Each vehicle directory includes two DXF files: one corresponding to the vehicle model name and a second file labeled "output.dxf." The latter is preferred for interactions with multibody systems due to its more uniform and simplified mesh. In addition, users may define custom vehicle dimensions. The specified vehicle geometry is used to determine the ellipsoid dimensions within the stiffness-based impact and rollover model and is also applied in collisions with multibody objects, unless a specific DXF/IDF shape is assigned for these contacts. Custom vehicle multibody models can also be defined for multibody-to-multibody interactions [34].

For stiffness-based impact modeling, the following parameters can be specified:

- Friction, representing the coefficient of friction of the vehicle body;
- Restitution, defined as the coefficient of restitution for vehicle impacts, with a single value applied when using the stiffness-based model;
- Stiffness, expressed as a deformation distance, where for passenger cars the specified value applies to the lower body structure, while one quarter of this stiffness is assigned to the roof region.

The multibody representation of the pedestrian consists of individual body segments (head, torso, pelvis, etc.), Fig. 5, interconnected by articulated joints that allow relative rotational motion. Each body's segment is characterized by distinct physical and mechanical properties, including geometry, mass, contact stiffness, and frictional behavior. The geometric shape of each segment is defined using a generalized ellipsoid of degree "n", which enables flexible representation of human body contours. Both pedestrian and occupant multibody models are typically composed of 20 rigid bodies connected through 19 joints, as described in [34]. The pedestrian can be modeled in any movement position; thus a wide variety of collisions can be simulated.

For each segment within the multibody system, the following properties may be independently defined:

- Body geometry, represented by ellipsoidal shapes, with configurable principal axis lengths and ellipsoid degree;
- Mass and corresponding moments of inertia for each rigid body;
- Contact stiffness coefficients used in the computation of interaction forces during impacts;
- Friction coefficients, differentiated between ellipsoid-to-vehicle contacts and ellipsoid-to-ellipsoid or ellipsoid-to-ground interactions.

Figure 5: The pedestrian multibody model.

In order to accurately simulate vehicle–pedestrian impacts, the pedestrian is modeled as a multibody system composed of rigid bodies interconnected by joints. Each body segment (e.g., head, torso, femur) is characterized by its geometry, mass properties, and contact parameters. This approach allows capturing complex kinematics and interaction forces during impact events. Each rigid body is defined in two coordinate systems an inertial (global) coordinate system, used for translational motion and a body-fixed coordinate system, aligned with the principal axes of the body [34].

Each body segment is represented by a generalized ellipsoid, Fig. 6, (superquadric) defined parametrically as:

$$\mathrm{P}(u,v) = \begin{pmatrix} X_e(u,v) \\ Y_e(u,v) \\ Z_e(u,v) \end{pmatrix} \tag{6}$$

$$X_e(u,v) = a \cdot \cos^{\frac{2}{n}}(v) \cdot \cos^{\frac{2}{n}}(u) \tag{7}$$

$$Y_e(u,v) = b \cdot \cos^{\frac{2}{n}}(v) \cdot \sin^{\frac{2}{n}}(u) \tag{8}$$

$$Z_e(u,v) = c \cdot \sin^{\frac{2}{n}}(v) \tag{9}$$

where:

- a, b, c are the semi-axes of the ellipsoid,
- n is the shape exponent controlling the curvature,
- $u \in [-\pi, \pi]$, $v \in [-\frac{\pi}{2}, \frac{\pi}{2}]$.

The corresponding outward normal vector is given by:

$$\mathrm{n}(u,v) = \frac{1}{a}\cos^{2-\frac{2}{n}}(v)\cos^{2-\frac{2}{n}}(u)\mathrm{i} + \frac{1}{b}\cos^{2-\frac{2}{n}}(v)\sin^{2-\frac{2}{n}}(u)\mathrm{j} + \frac{1}{c}\sin^{2-\frac{2}{n}}(v)\mathrm{k} \tag{10}$$

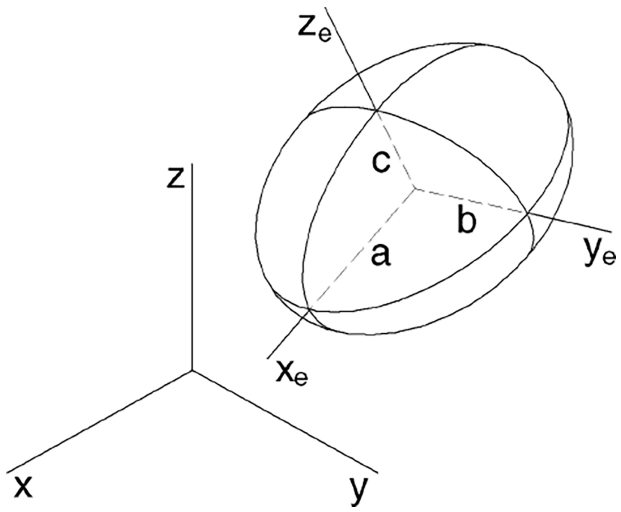

Figure 6: The coordinate systems of ellipsoid bodies [34].

This formulation enables efficient computation of contact detection, penetration depth, and surface normals, which are essential for impact modeling.

The motion of each rigid body i is governed by the Newton–Euler equations.

Translational motion:

$$m_i \ddot{\mathrm{x}}_i = \sum_j \mathrm{F}_j \tag{11}$$

Rotational motion:

$$\Theta_i \dot{\omega}_i + \omega_i \times (\Theta_i \omega_i) = \sum_j \mathrm{M}_j \tag{12}$$

where:

- m_i is the mass of body i,
- x_i is the position of the center of gravity,
- F_j are external forces (gravity, contact, joint forces),
- ω_i is angular velocity,
- $\dot{\omega}_i$ is angular acceleration,
- M_j are external moments,
- Θ_i is the inertia tensor:

$$\Theta_i = \begin{pmatrix} I_{xx} & -I_{xy} & -I_{xz} \\ -I_{xy} & I_{yy} & -I_{yz} \\ -I_{xz} & -I_{yz} & I_{zz} \end{pmatrix} \tag{13}$$

The system is solved numerically using an explicit Euler integration scheme with a small time step (typically 0.1–1 ms) to ensure stability in highly dynamic contact scenarios.

Rigid bodies are connected via ball-and-socket joints, Fig. 7, enforcing kinematic constraints through reaction forces.

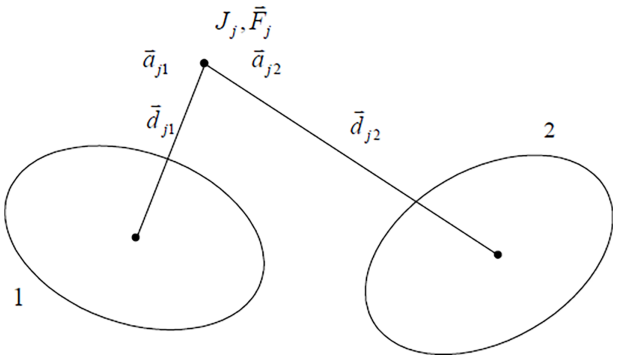

Figure 7: Joint definition [34].

At each time step, the following conditions must be satisfied:

- Action–reaction principle:

$$\mathrm{F}_{ij} = -\mathrm{F}_{ji} \tag{14}$$

- Acceleration compatibility:

$$\mathrm{a}_i = \mathrm{a}_j \tag{15}$$

The joint forces are obtained by solving a linear system:

$$\mathrm{A} \cdot \mathrm{F} = \mathrm{b} \tag{16}$$

or explicitly:

$$\begin{pmatrix} \mathrm{a}_{1,1} - \mathrm{a}_{1,2} \\ \mathrm{a}_{2,1} - \mathrm{a}_{2,2} \\ \vdots \\ \mathrm{a}_{j,1} - \mathrm{a}_{j,2} \end{pmatrix} = \mathrm{A} \begin{pmatrix} \mathrm{F}_1 \\ \mathrm{F}_2 \\ \vdots \\ \mathrm{F}_j \end{pmatrix} \tag{17}$$

where:

- A is a $3n \times 3n$ matrix,
- F_j are joint reaction forces,
- $\mathrm{a}_{j,1}, \mathrm{a}_{j,2}$ are accelerations at the joint for the connected bodies.

This approach is equivalent to the Lagrange multiplier method, where geometric constraints are replaced by constraint forces.

The contact models, based on a linear stiffness function, are used to calculate the contact forces between two multibody bodies or a body and another object. A coefficient of restitution is specified to define the amount of elasticity during the contact. Once the contact normal force is calculated friction forces are calculated, using the specified contact friction between the two bodies. Therefore sliding impacts, partially sliding impacts and full impacts can be calculated. Calculation of the amount of penetration, the location of the point of impact and the orientation of the contact plane is performed automatically. There is no need for user interaction for the calculation of these impacts once the general body parameters have been specified. Contact forces are computed using a linear stiffness penetration model.

Normal contact force is expressed:

- during approach:

$$F_n = \lambda \cdot S \tag{18}$$

- during separation:

$$F_n = \varepsilon^2 \cdot \lambda \cdot S \tag{19}$$

where:

- λ is penetration depth,
- S is the stiffness coefficient,
- ε is the coefficient of restitution.

For ellipsoid to ellipsoid contacts, Fig. 8, the assumption is made that the point of contact is found on a line between two points, where one point is on the surface of the first ellipsoid and the second point is on the surface of the other ellipsoid. The tangential planes for both points are parallel and the distance between these two planes is a minimum. The exact location of the point of contact can be found using the body stiffness values.

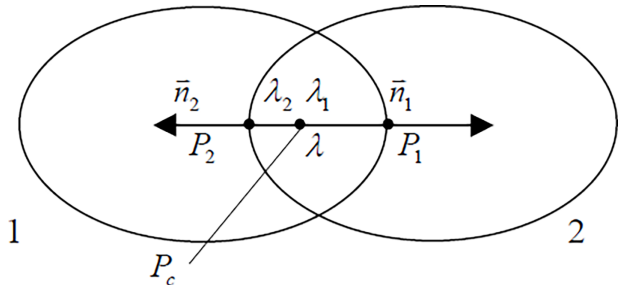

Figure 8: Elipsoid to elipsoid contact [34].

For two contacting bodies the geometric conditions is:

$$n_1 = -n_2 \tag{20}$$

$$\lambda = | P_1 - P_2 | = \lambda_1 + \lambda_2 \tag{21}$$

The penetration is minimized:

$$\lambda \rightarrow \min \tag{22}$$

Normal forces on the two surfaces:

$$F_{n1} = -\lambda_1 S_1 n_1 \tag{23}$$

$$F_{n2} = -\lambda_2 S_2 n_2 \tag{24}$$

The contact point is defined as:

$$P_c = P_1 - n_1 \lambda_1 = P_2 - n_2 \lambda_2 \tag{25}$$

Friction forces

$$\mu_c = \min(\mu_1, \mu_2) \tag{26}$$

$$F_{t1} = |F_{n1}| \cdot \mu_c \cdot \frac{v_{rel}}{|v_{rel}|} \tag{27}$$

Multibody forensic models are notably simpler models as they have fewer body segments a more simplified contact characteristics and do not necessitate long time for computation. A finite element pedestrian model lack of robustness during extended simulations, because is primarily subjected to the accumulation of explicit time-integration errors. The major advantage of Multibody models is that they can be easily scaled to any given stature or mass. An additional advantage of these models is that they are part of robust software packages [24]. A comparison of the motion response of their custom multibody model, which was based on the PC-CRASH solver, against video frames obtained from cadaveric and dummy tests, was conducted in [36]. The study involved adjusting the physical parameters, specifically the coefficients of restitution and friction, of the initially proposed model. These parameters were fine-tuned individually for each collision configuration in order to achieve a motion response that closely matched the reference test results.

4 Simulation Hypothesis

The simulations were performed in a three-dimensional environment. Throughout the analysis, vehicle–pedestrian collisions were simulated at various vehicle impact speeds. These scenarios were modeled by defining and applying the following initial conditions:

- The types of vehicles involved in the collision were the following: super-mini class-SM, compact class-CC, small SSUV, executive class-EC, VAN and ROBO. The characteristics of each vehicle is presented in Table 3;
- The selected impact speed of 40 km/h is consistent with widely adopted pedestrian safety assessment protocols, such as EuroNCAP testing conditions, where this velocity represents a critical and standardized scenario for evaluating pedestrian injury mechanisms. The use of a fixed impact speed allows a controlled comparison between vehicle geometries by eliminating additional variability associated with speed-dependent effects;
- Vehicle deceleration during impact 5 m/s^2;
- Additional simulations were conducted for three distinct braking deceleration levels in order to perform a sensitivity analysis of pedestrian throw distance.
- A standard 50th percentile adult male pedestrian configuration was used in this study, consistent with common accident reconstruction practice, characterized by a height of approximately 1.75 m and a mass of about 78 kg. The multibody framework allows scaling of anthropometric characteristics (e.g., height and mass), enabling the simulation of different pedestrian statures and initial conditions;
- Simulations of pedestrian projection distance were performed for three pedestrian masses and three heights to evaluate sensitivity effects.
- Pedestrian walking perpendicular to vehicle direction at 1.4 m/s;
- The impact occurred with the median area of the bumper (on the longitudinal axis of the vehicle), the area thus considered is the most favorable in terms of the severity of the pedestrian's injuries;
- The coefficient of friction between vehicle and pedestrian is 0.2;
- In this study, force-based metrics are interpreted as relative indicators of mechanical loading, enabling comparison across different vehicle geometries. The conclusions are therefore based on observed shifts in loading patterns rather than absolute injury risk.

The simulation framework employed in this study is based on controlled and standardized assumptions, designed to isolate the influence of vehicle front-end geometry on pedestrian injury mechanisms. The selected impact speed of 40 km/h follows commonly adopted pedestrian safety testing conditions (e.g., EuroNCAP), while pedestrian motion, friction coefficients, and impact configuration are defined according to validated literature values. These assumptions ensure consistency across all simulated scenarios and enable a direct comparative analysis between vehicle geometries. Consequently, the objective of this study is not to provide absolute injury predictions for specific real-world cases, but rather to identify relative biomechanical trends and injury redistribution mechanisms.

5 Results

Ravani et al. classified pedestrian post-impact kinematics as one of the following conditions: wrap trajectory, forward projection, fender vault, roof vault or somersault [37]. Vehicle-pedestrian impacts create different movement patterns like those mentioned above, depending on vehicle speed, position of center of gravity of pedestrian in rapport with bonnet leading edge height, impact point front or corner and vehicle type. Roof vaults often involving the pedestrian going over the vehicle's roof, it is common in higher-speed collisions with certain vehicle profiles, leading to severe head injuries [38].

The severity of head injury is quantified using the Head Injury Criterion (HIC), according to [39], which is based on the time integral of the resultant head acceleration. The HIC is defined as:

$$HIC = max_{t_1,t_2}\left[(t_2 - t_1)\left(\frac{1}{t_2 - t_1}\int_{t_1}^{t_2} a(t)\,dt\right)^{2.5}\right] \tag{28}$$

where:

- $a(t)$ is the resultant acceleration of the head center of gravity expressed in units of gravity g,
- t_1 and t_2 define the time interval over which the criterion is maximized.

In practical applications, the duration of the time interval is limited to 15 ms for HIC_{15} and 36 ms for HIC_{36}.

$(t_2 - t_1) \leq 0.015$ or 0.036 s

The HIC value reflects both the magnitude and duration of head acceleration, making it sensitive to different impact profiles. Lower peak accelerations acting over longer durations may produce similar HIC values to short-duration high peaks, which explains the differences observed between vehicle geometries in this study. Good performance is considered when HIC values lower than 1000 are obtained in a pedestrian collision. The accelerations curves enabled the subsequent determination of the head injury criterion HIC, these values being synthesized in a table similar to Table 4.

In addition to head injury assessment, thoracic injury risk was evaluated using peak contact force and acceleration-based indicators.

The resultant thoracic force is defined as:

$$F_{thorax}(t) = \sqrt{F_x^2 + F_y^2 + F_z^2} \tag{29}$$

The peak thoracic force is then:

$$F_{thorax}^{max} = \max_t\left(F_{thorax}(t)\right) \tag{30}$$

Table 4: HIC values calculated, acceleration and forces during contact with vehicle.

No	Vehicle Type	HIC	HIC36	HIC15	Head Peak Acceleration [m/s^2]	Thorax Peak Forces [N]	Lower Limb Peak Forces [N]	Throw Distance [m]
1	SM	603	603	425	769	2987	3854	12.88
2	CC	760	760	545	888	5236	4222	13.19
3	SSUV	469	449	244	576	5854	7231	13.51
4	EC	438	420	255	620	7117	5160	13.00
5	VAN1	227	132	47	331	11,338	6384	18.12
6	VAN2	294	253	88	473	9500	8658	16.57
7	ROBO1	230	230	151	646	14,969	4858	17.17
8	ROBO1_low_cl	220	220	147	633	15,173	4910	17.32
9	ROBO1_wh	218	218	142	607	12,341	16,364	12.82
10	ROBO2	181	147	103	458	2917	8598	14.88

From a biomechanical perspective, thoracic injury is related to compression and energy transfer to the ribcage. A simplified relationship between force and chest deformation may be expressed as:

$$F_{thorax} = k_{chest} \cdot \delta_{chest} \tag{31}$$

where:

- k_{chest} is the effective thoracic stiffness,
- δ_{chest} is chest compression.

In a more general injury-risk framework, thoracic injury probability may be expressed as a function of normalized force or compression:

$$P_{injury} = f\left(\frac{F_{thorax}}{F_{crit}}\right) \tag{32}$$

or

$$P_{injury} = f(\delta_{chest}) \tag{33}$$

These formulations highlight that thoracic injury is governed by both force magnitude and deformation characteristics. Thoracic peak force is used in this study as a comparative indicator of loading severity rather than a direct injury predictor.

The vehicle front-end geometry, defined by parameters P1–P9, influences the pedestrian response through the determination of contact conditions. The geometric parameters define the spatial configuration of the vehicle front, which directly affects: the location of the contact point, the orientation of the contact normal, the timing and duration of contact. Thus, the mapping can be expressed conceptually as:

$\{\text{P1} \ldots \text{P9}\} \rightarrow$ contact point $\rightarrow$ contact normal $\rightarrow$ contact force $\rightarrow$ biomechanical response

This relationship explains how variations in bumper height, hood angle, and front profile lead to different pedestrian kinematics and injury mechanisms.

The method used to analyze the data stemmed from simulations was structured throughout the following stages:

- Carrying out an overall analysis of accelerations during the specific time interval;

- Determining time sub-intervals of high interest. These are characterized by the head acceleration values, contact forces on lower leg, thorax and head;
- Determining the values regarding the injury criteria;
- Carrying out a comparative analysis of these values in order to determine the influence of front end design parameters upon the impact with the pedestrian as well as the injury degree.

For the accuracy of the results, the model used has been validated in previous research in [17,19,40,41].

The impact scenario, identical for all the geometric typologies studied, in accordance with the previously mentioned hypotheses, included the stages of primary and secondary impact of the pedestrian with the vehicle, followed by the flight phase and finally rolling/sliding on the ground until the final position. As the final distance of throwing the pedestrian, we considered the thorax as the element that indicates the total distance of its projection. In all the cases analyzed, the total duration of the impact, until the pedestrian landed in the final position on the ground, was in the range of 2–2.5 s. The graph in Fig. 9 shows the total distance of pedestrians throwing, for the ten configurations of the frontal geometry. The largest projection distances are found in the cases VAN1 and VAN2, ROBO1 and ROBO1_low_clearance, probably due to both the larger masses of the vehicles and the type of impact, forward projection, different from that of vehicles with a "classic" profile where the type of impact is (wrap around or sommersault). Atypical case ROBO1_wheel, where the throw distance is among the smallest, due to the impact with the lower limbs.

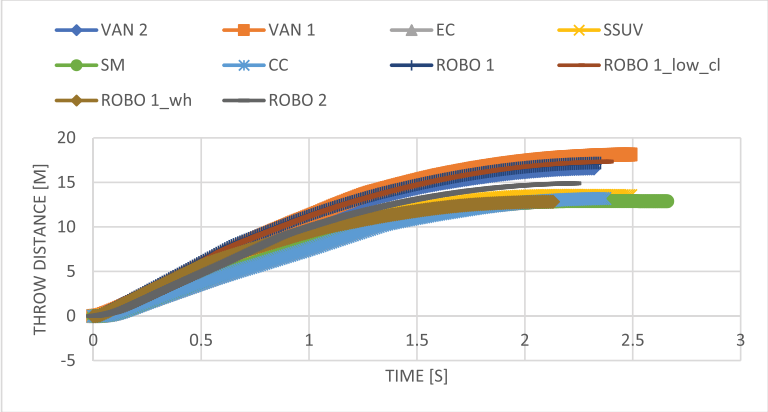

Figure 9: Pedestrian throwing distance, according to frontal geometry typology.

After the primary and secondary vehicle contacts, the pedestrian may enter a flight phase, followed by a ground-contact phase. During this final phase, the body may undergo sliding, rolling, and successive contacts with the ground, with random motion characteristics and variable energy dissipation. Therefore, a direct and universal correlation between throw distance and injury severity cannot be established. Each accident remains case-specific, because injury outcomes are strongly affected by the contact conditions during ground impact, including the type and state of the surface, such as asphalt, compact soil, loose soil, snow, or ice, as well as the possible presence of local obstacles such as curbs, poles, trees, or roadside objects. Consequently, in the present study, throw distance is used only to support the interpretation of pedestrian kinematics and energy transfer, while injury severity is discussed through biomechanical loading indicators obtained from the simulations.

The impact with the lower limbs differs, depending on the leg that was hit first by the vehicle and depending on the posture in which it is (with which leg it steps forward), Figs. 10 and 11. The duration of the action of the forces is a maximum of 50 ms. Higher values of the forces are observed on the leg that is

hit first, Fig. 10. It is worth mentioning the higher value of the forces with the increase in the height of the contact point between the vehicle and the leg (shock absorber). On the leg that is not hit first, the force values are lower, and the time at which the forces begin to be applied has a delay of approximately 10 ms compared to the limb hit first. Atypical case, ROBO1_wheel, where it is observed that the impact on the standing leg has a maximum at 20 ms, slightly later, compared to the other types of vehicles. In the first 10 ms, the left leg is dragged on the ground. In the cases ROBO1 and ROBO1_low_cl, due to vehicle flat and slightly inclined profile, the primary impact is in the tibia-ankle area, leading to a lower effort on the left femur.

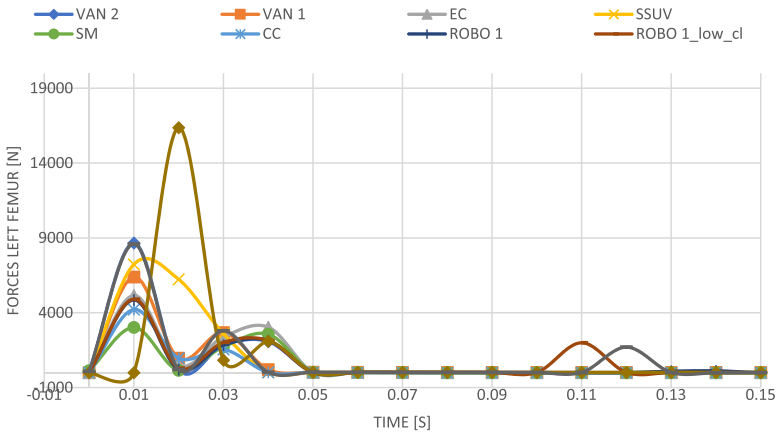

Figure 10: Contact forces at the left foot (the foot struck first in the case of simulations).

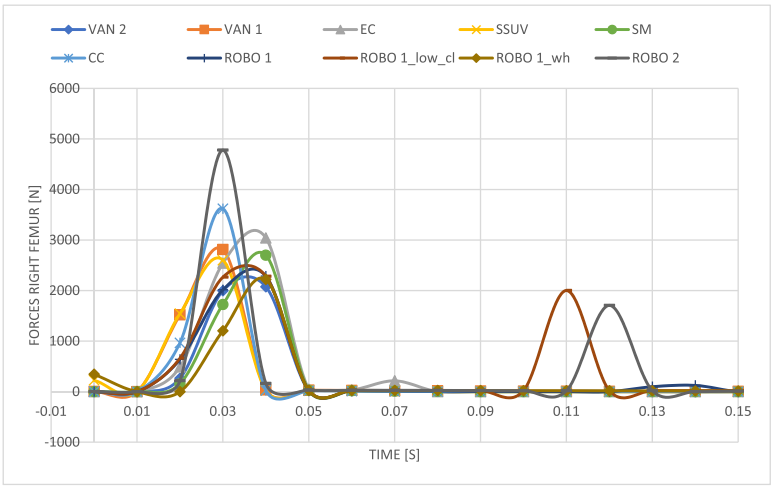

Figure 11: Contact forces at the right foot.

The contact of the chest with the vehicle extends for a maximum of 0.15 s, Figs. 12 and 13, from the primary impact and differs depending on the shape of the vehicle. From Figs. 12 and 13 it can be seen that for vehicles in classes SM, CC, EC, the impact of the chest with the hood area occurs approximately 0.11 s after the impact on the foot. The SSUV class generates accelerations and forces on the chest of the adult pedestrian comparable in value to the SM, CC, EC classes and the maximum forces and accelerations occur slightly earlier, at the time 0.08 s. Vehicles in classes VAN1, VAN2, ROBO1, through their frontal profile produce the impact with the chest almost at the same time as the primary impact on the lower limbs, Figs. 10–12. The values of forces and accelerations upon contact with the vehicle are higher than in classes SM, CC, SSUV,

EC. Classes ROBO1, VAN1, VAN2 have the highest contact forces. and accelerations in the chest area, a likely factor being the greater mass of the vehicles.

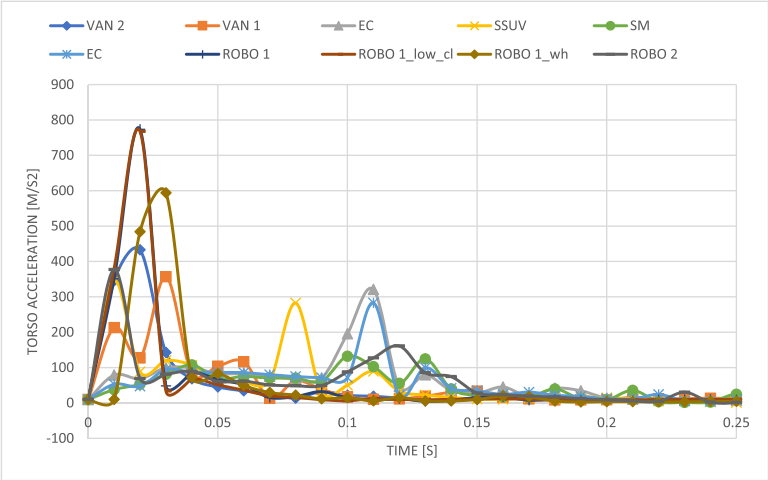

Figure 12: Torso accelerations.

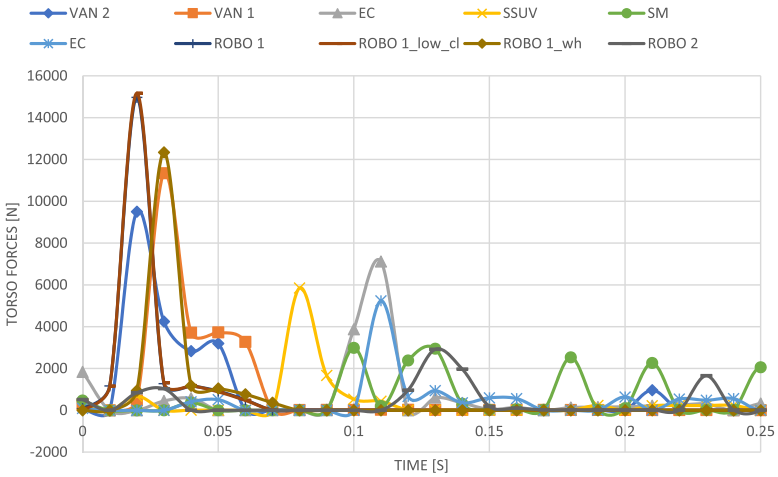

Figure 13: Torso forces.

ROBO1, VAN1 and VAN2 type vehicles cause the head to hit the vehicle body faster in time, between 0.03 and 0.08 s, compared to the "classic" forms, Fig. 14. The impact in the head area for the VAN1 and VAN2 typologies produce the lowest decelerations in value, but longer in duration. Although the ROBO1 typology, with all its analyzed variants, generates higher peaks in amplitude of head accelerations, these are limited in duration of action, thus the HIC values are low. The evolution of forces and accelerations, on the entire human body shows that most of the impact energy is taken over by the lower limbs and thorax, for the VAN1, VAN2 and ROBO1 classes. Numerical values regarding the impact of the pedestrian's body are presented in Table 4.

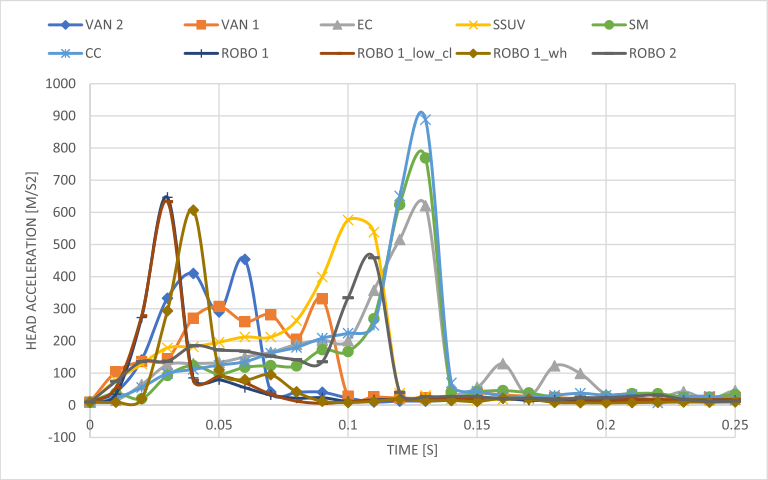

Figure 14: Head accelerations.

6 Discussion

The results are derived from deterministic simulation scenarios, intentionally structured to highlight systematic differences between vehicle configurations. In this context, statistical variability is not explicitly modeled, as the study does not rely on stochastic inputs. Instead, robustness is supported by the consistency of observed trends across multiple vehicle typologies. Future work will extend this approach using probabilistic simulations to quantify variability under real-world conditions.

The surface of the area defined by the hood–fender–windshield assembly can be characterized by regions with different potentials for head and torso injury to pedestrians, as illustrated in Fig. 15. These regions include: the central area of the hood, the hood–fender zone, which comprises the hood surface bounded within 150 mm of its lateral edges, as well as the rear portion of the hood located between the lower edge of the windshield and an imaginary line positioned 150 mm from the rear edge of the hood.

During traffic accidents involving pedestrians, impacts with the vehicle occur in a largely random manner within these regions. Depending on the vehicle speed and front-end profile, the pedestrian may experience contact with the windshield or, in more severe cases, with the A-pillars.

Through a retrospective examination of the evolution of pedestrian protection, it can be observed that the severity of pedestrian injuries has decreased substantially over time. This improvement has been driven by changes in vehicle architecture as well as by constructive and technological innovations. Fig. 16 illustrates, from left to right, the temporal evolution of the front-end geometric zones of a passenger vehicle and their associated potential for pedestrian injury (red = severe injuries, green = minor injuries).

In the past, impacts with the central region of the hood generated high values of the HIC, as shown in Fig. 16. In modern vehicles, impacts occurring in the central hood area result in lower HIC values compared to those measured in the frontal edge region and in the vicinity of the A-pillars. In the hood–fender zone, the head injury criterion values are comparable to those observed in the other hood regions defined above, Fig. 16, despite the presence of rigid structural components such as fender mounting points, suspension attachments, and local reinforcements. Owing to improved fender attachment and structural design solutions, impact forces in this area are reduced when compared with those observed in older vehicles of similar class, as illustrated in Fig. 17.

Figure 15: Delimitation of areas with different potential for injury on the front surface of the vehicle.

Figure 16: Level of injury to pedestrians by the front surface of a car, evolution over time (adapted from EuroNCAP).

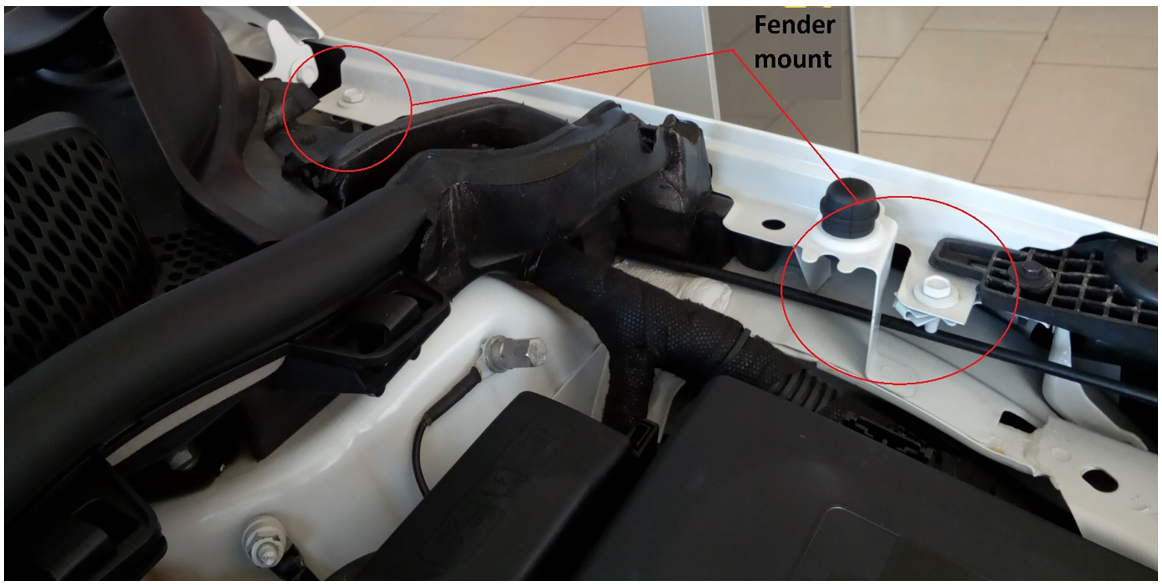

Figure 17: Wing attachment through deformable, slightly rigid elements.

Another vehicle characteristic that influences impact severity is the clearance between the hood surface and the components located in the engine compartment, as well as the material used for the hood and its

reinforcement structure. In order to maintain low HIC values, sufficient space must exist between the hood and the powertrain components. In most cases, these components are rigid and massive when compared to the pedestrian's head and the material of the hood itself.

The materials used in vehicle components also play an important role in determining the severity of pedestrian injuries in the context of external passive safety. Conventional steel sheet metal used for hood and fender structures is capable of absorbing impact energy, thereby generating lower contact forces and, consequently, reduced injury criterion values. Aluminium hoods also exhibit good energy-absorption characteristics; however, they tend to undergo larger deformations, which necessitates increased clearance between the hood and the underlying vehicle subassemblies. The hood reinforcement structure further affects pedestrian injury severity during hood impacts. Vehicles equipped with hoods featuring rigid reinforcement structures, Fig. 18a may lead to more severe pedestrian injuries compared to those with more compliant reinforcement designs, Fig. 18b.

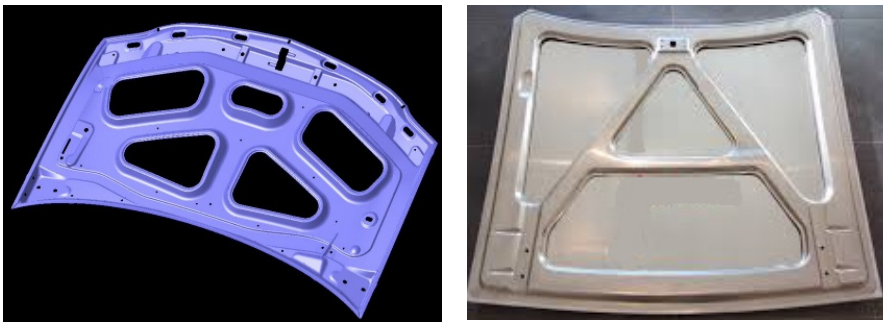

Figure 18: Reinforcement structure for the hood: (**a**) rigid, (**b**) flexible.

Vehicle geometry fundamentally alters pedestrian kinematics, force transmission pathways, and injury distribution. Rather than uniformly increasing or decreasing injury severity, emerging autonomous vehicle architectures redistribute injury risk between head and thoracic regions. This redistribution has important implications for pedestrian safety assessment frameworks that currently emphasize head injury criteria. The most important result is the inverse relationship observed between head injury metrics (HIC) and thoracic loading across vehicle geometries. Conventional passenger vehicles (SM and CC) produced the highest HIC values (603–760), consistent with classical wrap-around kinematics in which the pedestrian rotates onto the hood and windshield. These configurations delay torso contact (~0.11 s after lower limb impact), allowing rotational motion to develop and resulting in elevated head deceleration.

In contrast, vertically oriented or flat-front designs (VAN1, VAN2, ROBO1, ROBO2) produced substantially lower HIC values (181–368) but markedly increased thoracic peak forces, except ROBO2. The ROBO1 configuration generated thoracic forces exceeding 15 kN, approximately three to five times greater than those observed in classical passenger vehicles. This shift reflects immediate torso engagement and suppression of wrap-around kinematics.

These results suggest that vertical front-end geometries reduce rotational head loading while increasing direct chest compression. The trade-off observed here indicates that improvements in HIC do not necessarily reflect overall reductions in pedestrian injury risk. Instead, injury mechanisms are redistributed spatially and temporally.

Timing differences across configurations provide insight into the biomechanical mechanisms underlying injury redistribution. In classical geometries, lower limb contact precedes thoracic engagement by

approximately 0.1 s, facilitating angular acceleration of the upper body and head impact against compliant hood or windshield regions. In vertical autonomous designs, thoracic contact occurs almost simultaneously with lower limb impact, limiting rotation and producing a forward projection trajectory. Throw-distance analysis supports this interpretation. VAN1, VAN2, and ROBO1, except ROBO1_wheel, configurations produced the largest projection distances, consistent with translational rather than rotational energy transfer.

These patterns align with prior kinematic classifications (e.g., forward projection vs. wrap trajectory) and suggest that front-end verticality governs post-impact motion more strongly than vehicle mass alone.

Although heavier vehicles exhibited greater projection distances, mass did not consistently predict injury metrics. For example, the executive-class vehicle EC, 2135 kg produced higher HIC and thoracic forces than lighter vehicles, but the extreme thoracic loading observed in ROBO1 was primarily attributable to geometry rather than mass. This finding reinforces the dominant role of front-end profile in shaping injury mechanisms.

Lower-limb force analysis revealed rapid peak loading within the first 50 ms of impact, with the initially struck limb experiencing the highest forces. Elevated bumper height increased lower limb peak forces, consistent with prior biomechanical findings. Notably, the ROBO1_wh configuration, representing wheel-first contact, produced the highest lower limb peak force, 16,364 N.

Passenger car tire vertical stiffness typically varies significantly with inflation pressure, wheel load and tire construction. Some values used in studies is in range of 181–235 N/mm [42] and 195–400 N/mm [43]. For pedestrian safety, total bumper/spoiler stiffness, in order to manage injury metrics, like lower leg acceleration, used in literature is in range of 2207.25 N/mm in [44] and in range 650 up to 810 N/mm, for deflection of 6 and 10 mm for fascia bumper, in [45]. Thus, in the case of vehicles whose design resembles the Zoox, the impact of the pedestrian with the wheel itself should not cause greater injuries than the classic structure of a crash bar. However, the kinematics of the pedestrian may change due to the fact that the impact at the foot is made with a material that has greater elasticity than the front structure of the crash bar. Although passenger car tire stiffness values reported in the literature are not greater than typical bumper stiffness, altered impact geometry modifies kinematic response and load distribution. Wheel-first contact may therefore introduce injury mechanisms not adequately represented in existing regulatory test configurations, which typically assume bumper-first engagement.

This finding highlights a potential gap in current pedestrian protection protocols for symmetric, wheel-exposed autonomous vehicle platforms.

Head acceleration traces demonstrate distinct amplitude–duration characteristics across vehicle types. VAN1 and VAN2 configurations produced lower peak head accelerations but longer deceleration durations, resulting in reduced HIC values. ROBO1 configurations exhibited higher instantaneous acceleration peaks but shorter duration, also yielding lower HIC values. These patterns illustrate the sensitivity of HIC to both magnitude and temporal integration. While HIC values across all configurations remained below the 1000 threshold, substantial differences were observed between classical passenger vehicles (highest HIC) and autonomous flat-front designs (lowest HIC). However, the concomitant increase in thoracic loading suggests that reliance on HIC alone may not adequately characterize injury risk in emerging vehicle geometries.

In current vehicle designs, sensing systems are typically embedded within the vehicle structure, rather than mounted as external protruding elements. This is done to ensure both aesthetic integration and aerodynamic performance. Therefore, sensors do not necessarily introduce significant visible geometric changes to the vehicle front-end. In the present study, sensor placement was not explicitly modeled. The related discussion refers only to potential design implications, particularly regarding localized stiffness variations, and not to directly simulated features.

The influence of hood clearance, reinforcement stiffness, and structural compliance discussed in the manuscript is supported by the simulation outcomes. Increased under-hood clearance and compliant reinforcement structures are associated with lower head deceleration, consistent with established pedestrian protection principles. Electric autonomous platforms may provide additional design flexibility due to reduced engine packaging constraints. However, flat and vertical front-end symmetry, along with integrated sensor housings, introduces localized stiffness regions that may influence injury outcomes. The ROBO1_wh case suggests that structural discontinuities can alter load transfer and peak force generation. A summary of the influence of the frontal profile of autonomous vehicles on pedestrian impact and injuries is presented in Table 5.

Table 5: Influence of autonomous vehicle front-end design on pedestrian injury biomechanics.

Front-End Design Element	Design Characteristics in Autonomous Vehicles	Observed Biomechanical Trend (Simulation-Based)	Influence on Injury Risk
Bumper height & compliance	Higher in VAN/ROBO1 platforms; vertical fascia	Increased direct torso engagement	Elevated thorax forces; altered lower limb loading
Hood leading edge height	Reduced hood projection in flat-front designs	Limited wrap-around kinematics	Lower HIC but increased chest compression
Hood length & slope	Shortened or nearly absent in symmetric designs	Reduced head impact velocity in modeled cases	Decreased HIC values
Windshield base stiffness	May remain rigid near cowl area. Integrated sensor housings may stiffen windshield area	Localized stiff zones increase head deceleration	Higher HIC in cases with upper contact
Sensor placement (LiDAR, radar)	External or embedded in front fascia	Lower leg injuries, Chest compression increases with vertical fronts	Hard sensor housings may create localized injury risk if struck
Vehicle overall frontal geometry (VAN-type)	Elevated, semi-vertical front	Direct torso impact; reduced head rotation	Lower HIC, higher thorax peak forces
Vehicle overall frontal geometry (ROBO1-type)	Flat, symmetric vertical front	Torso-dominant impact pattern	Very high thorax forces (>15 kN), moderate-to-low HIC
Localized structural stiffness	Reinforcements, sensor mounts	Can create local acceleration peaks	Potential HIC increase if head strikes stiff area
Under-hood clearance	Variable depending on EV packaging	Affects deformation energy absorption	Greater clearance reduces HIC, reduce thorax injuries
Thorax injury mechanism	Dependent on front height and stiffness distribution	Chest compression increases with vertical fronts	Elevated thoracic trauma risk

(Continued)

Table 5 (continued)

Front-End Design Element	Design Characteristics in Autonomous Vehicles	Observed Biomechanical Trend (Simulation-Based)	Influence on Injury Risk
Head Injury Criterion (HIC) response	Geometry-dependent	Wrap kinematics increase HIC; direct torso impact reduces it	Trade-off between head and thorax injury mechanisms

The findings are applicable across a broad range of vehicle categories, including conventional passenger vehicles, electric vehicles, and larger platforms such as vans or trucks. Electric vehicle architectures, in particular, provide increased design flexibility due to reduced engine packaging constraints, potentially enabling improved energy absorption characteristics.

The increasing design flexibility of electric vehicle may allow improved pedestrian protection through enhanced deformation space. In particular, increased under-hood clearance and energy-absorbing structures are known to reduce head injury metrics by allowing controlled deformation during impact. Electric vehicle platforms may offer additional design flexibility in this regard due to reduced engine packaging constraints.

Conversely, vehicles with higher and more vertical front-end geometries tend to promote direct torso engagement, resulting in increased thoracic loading. These observations indicate that pedestrian injury criteria must be adaptable to diverse vehicle architectures and should not rely exclusively on head-based metrics, especially in the context of autonomous vehicles.

The ROBO1 and ROBO2 configurations represent two distinct interpretations of non-classical autonomous vehicle front-end design. Although both employ symmetric and relatively vertical frontal architectures, their biomechanical responses differ substantially.

With respect to head injury metrics, the ROBO2 configuration demonstrated the most favorable performance among all vehicles tested (HIC = 181; HIC36 = 147; HIC15 = 103). In comparison, the ROBO1 configuration produced also low HIC values (230), with similar results for ROBO1_low_clearance (220) and ROBO1_wh (218). These values remain below those observed for compact passenger vehicles, CC (760), indicating that both autonomous geometries reduce wrap-around kinematics relative to conventional sloped designs. However, ROBO2 more effectively attenuates head deceleration magnitude and duration, suggesting improved energy absorption or more favorable upper-body rotation control.

The principal difference between the two configurations emerges in thoracic loading. ROBO1 generated the highest thorax peak force recorded in the study (14,969 N), with ROBO1_low_cl and ROBO1_wh also producing elevated forces (15,173 and 12,341 N, respectively). These values substantially exceed those observed in conventional passenger vehicles and indicate a torso-dominant impact mechanism characterized by early and direct chest engagement. In contrast, ROBO2 produced a thorax peak force of 2917 N, comparable to the super-mini class and markedly lower than ROBO1. This suggests that vertical symmetry alone does not determine thoracic risk; rather, the interaction between bumper height, compliance, and stiffness distribution governs chest compression severity.

Lower-limb loading further differentiates the two platforms. ROBO1_wh exhibited the highest lower-limb force (16,364 N), reflecting the atypical wheel-first contact scenario. ROBO2, however, demonstrated elevated lower-limb loading (8598 N) without corresponding extreme thoracic forces, implying greater energy redistribution to the extremities. This may delay torso engagement and reduce chest compression.

In the present study, the significantly higher thoracic forces observed for vertical and flat-front geometries indicate a shift toward compression-dominated injury mechanisms, in contrast with rotation-dominated head injury mechanisms in conventional vehicles.

A synthesis, in Table 6, shows that conventional passenger cars promote a wrap-around trajectory characterized by body rotation over the bonnet and dominant head involvement, Fig. 19.

Table 6: Comparative synthesis of pedestrian impact kinematics for different vehicle front-end geometries.

Parameter	Passenger Cars (SM-CC-EC-SSUV)	Vans (VAN1-VAN2)	Autonomous Vehicles (ROBO1-ROBO2)
Front-end geometry	Low bonnet, sloped hood surface	High and more vertical front structure	Flat, highly vertical and symmetric frontal architecture
Initial contact location	Lower limbs (bumper–leg contact)	Lower limbs followed rapidly by pelvis contact	Lower limbs followed rapidly by pelvis contact; Lower limbs or wheel area depending on geometry
Contact phase	Pelvis and thorax sliding over the bonnet	Immediate thorax-torso engagement with frontal panel	Immediate thorax-torso engagement with flat frontal surface
Pedestrian body motion	Progressive rotation over the hood	Limited rotation; pedestrian pushed forward	Rotation largely suppressed; body remains upright initially
Dominant kinematic mechanism	Wrap-around trajectory	Forward projection trajectory; Thorax-torso dominant impact pattern	Forward projection trajectory; Thorax-torso dominant impact pattern
Head impact probability	High contact with bonnet or windshield	Reduced compared with passenger cars	Reduced or delayed depending on geometry
Thoracic loading	Moderate	High due to early chest contact	High due to direct torso engagement
Lower limb loading	Significant but localized at bumper level	Increased due to higher bumper height	Potentially increased, especially in wheel-first contact scenarios
Pedestrian trajectory after impact	Rotation over hood followed by ground contact	Forward projection away from vehicle	Sliding or forward projection depending on front structure
Overall injury distribution trend	Head-dominated injury mechanism	Thorax-dominated injury mechanism, lower limb	Redistribution toward thorax and lower limbs

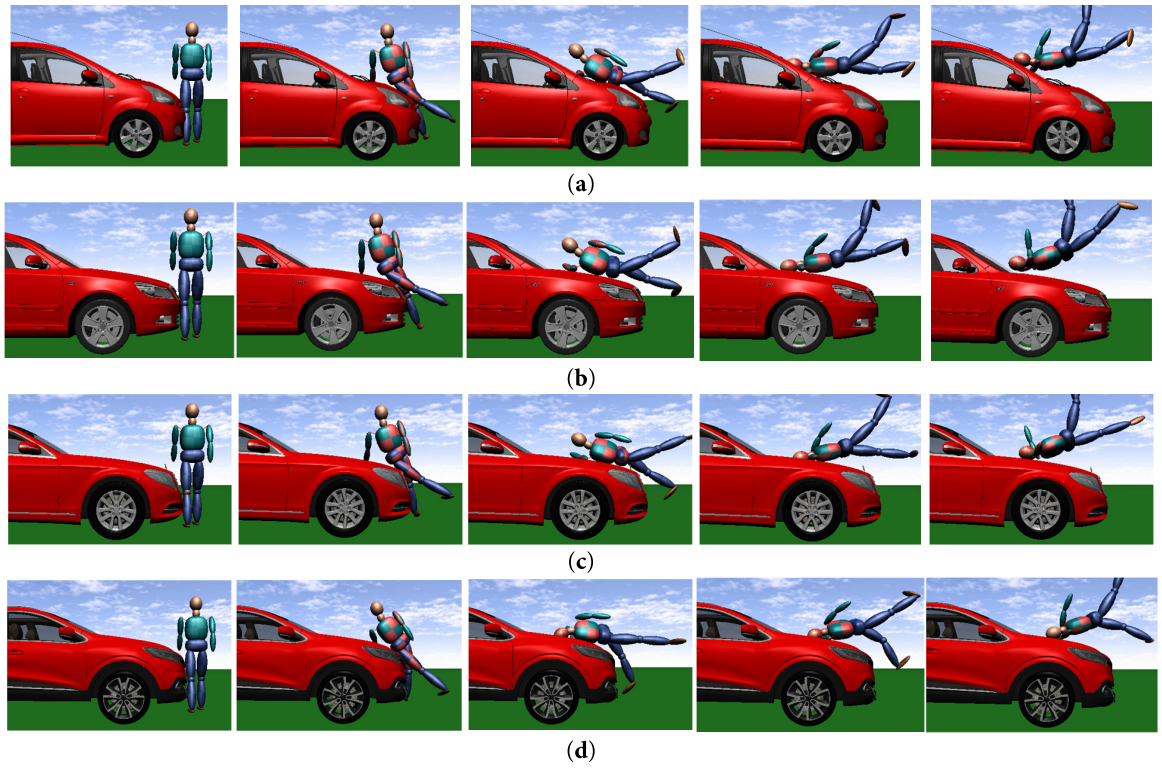

Figure 19: Pedestrian trajectory for (**a**)—SM, (**b**)—CC, (**c**)—EC, (**d**)—SSUV class vehicle.

Vehicles with higher front ends, such as vans, produce early thoracic engagement and forward pedestrian projection, Fig. 20.

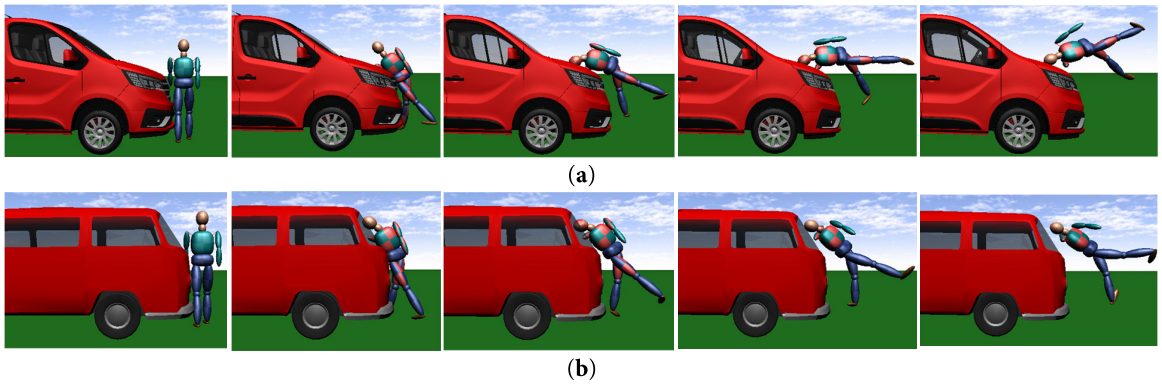

Figure 20: Pedestrian trajectory for (**a**)—VAN1 and (**b**)—VAN2 class vehicle.

Emerging autonomous vehicle architectures with flat vertical fronts suppress wrap-around motion and redistribute loading toward the torso and lower limbs, Fig. 21.

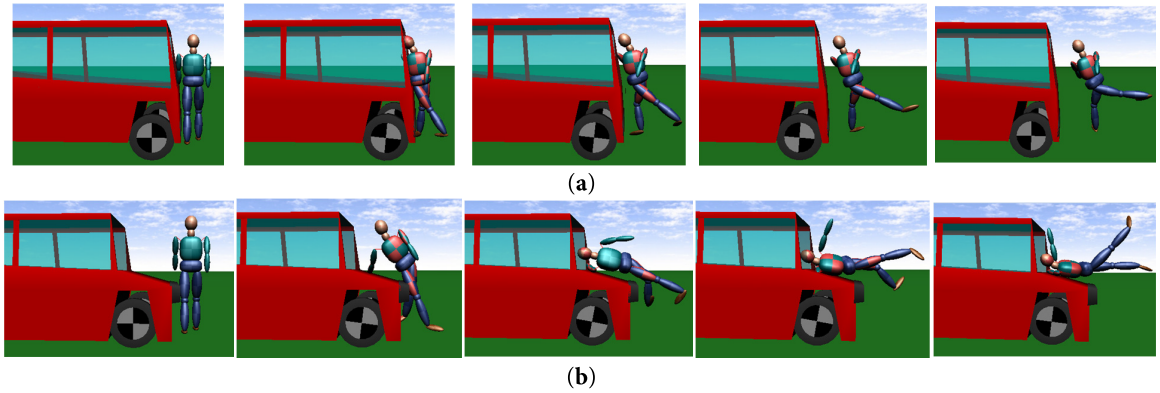

Figure 21: Pedestrian trajectory for (**a**)—ROBO1 and (**b**)—ROBO2 class vehicle.

In terms of pedestrian projection distance, a sensitivity analysis was performed considering different pedestrian masses, different pedestrian heights, and three distinct braking deceleration levels.

The influence of pedestrian mass on projection distance was analyzed for identical anthropometric height but varying body mass (55, 75, and 115 kg), Table 7. The results consistently show that lighter pedestrians tend to be projected over longer distances, while heavier pedestrians exhibit shorter projection trajectories. This behavior can be explained by the momentum transfer during impact. For a given vehicle mass and velocity, a lighter pedestrian undergoes a higher acceleration and achieves a higher post-impact velocity, leading to an increased projection distance. In contrast, heavier pedestrians absorb a larger portion of the impact energy and exhibit lower acceleration, resulting in shorter projection distances.

Table 7: Sensitivity analysis of pedestrian mass on throw distance.

Vehicle	Throw Distance for Pedestrian 115 kg [m]	Throw Distance for Pedestrian 75 kg [m]	Throw Distance for Pedestrian 55 kg [m]	Tendency
SM	11.3	12.9	13.0	Decrease with mass
CC	13.5	13.2	13.4	Almost constant
EC	12.6	13.0	13.3	Slight decrease
SSUV	13.0	13.5	13.6	Slight decrease
VAN1	16.6	18.1	17.9	Decrease with mass
VAN2	16.0	16.6	16.8	Decrease with mass
ROBO1	17.0	17.8	18.1	Decrease with mass
ROBO1_low_cl	17.2	17.7	18.4	Decrease with mass
ROBO2	14.1	14.8	15.1	Decrease with mass

The results in Table 8 indicate that pedestrian height has a significant influence on projection distance, with the effect strongly dependent on vehicle front-end geometry. For conventional passenger vehicles with sloped front profiles, shorter pedestrians tend to experience larger projection distances due to increased rotational motion (wrap-around mechanism). In contrast, for vehicles with flat or vertical front geometries, taller pedestrians exhibit greater projection distances, as the impact occurs closer to the center of mass, promoting forward translational motion rather than rotation. These findings highlight that pedestrian height

primarily affects the kinematic impact mechanism rather than acting as a simple scaling factor, leading to fundamentally different projection behaviors depending on vehicle geometry.

Table 8: Sensitivity analysis of pedestrian height on throw distance.

Vehicle	Throw Distance for Pedestrian 155 cm [m]	Throw Distance for Pedestrian 175 cm [m]	Throw Distance for Pedestrian 200 cm [m]	Tendency
SS	13.0 m	12.8 m	11.9 m	Decrease
CC	13.7 m	13.1 m	13.2 m	Slightly decrease
EC	13.7 m	13.0 m	12.6 m	Decrease
SSUV	15.2 m	13.5 m	12.6 m	Decrease
VAN1	17.2 m	18.1 m	16.3 m	Maxim at 175 cm
VAN2	16.2 m	16.5 m	16.9 m	Increase
ROBO1	16.1 m	17.8 m	18.0 m	Increase
ROBO1_low_cl	15.6 m	17.8 m	17.6 m	Increase
ROBO2	14.1 m	14.9 m	17.5 m	Increase

The analysis of the projection distance clearly highlights the influence of braking deceleration on pedestrian kinematics, Table 9. In general, increasing the deceleration level from 2.5 to 7.5 m/s^2 leads to a consistent reduction in projection distance, with decreases ranging from approximately 3% up to 45%, depending on vehicle geometry. For conventional passenger cars (e.g., sedan and compact vehicles), the reduction is significant (25%–45%), indicating that braking plays a major role in limiting pedestrian throw distance. In contrast, for vehicles with more vertical front-end geometries (e.g., vans or autonomous box-shaped designs), the projection distance shows minimal sensitivity to braking deceleration (below 10%).

Table 9: Sensitivity analysis of vehicle deceleration on pedestrian throw distance.

Vehicle	Throw Distance at 2.5 m/s^2 [m]	Throw Distance at 5 m/s^2 [m]	Throw Distance at 7.5 m/s^2 [m]	Variation (%)
SM	14.6	12.9	10.9	~25%
CC	20.0	13.2	11.0	~45%
EC	15.3	13.0	10.9	~29%
SSUV	15.5	13.5	13.0	~16%
VAN1	18.0	17.5	17.0	~6%
VAN2	17.0	16.5	16.3	~4%
ROBO1	17.8	17.6	17.3	~3%
ROBO1_low_cl	18.3	18.0	17.8	~3%
ROBO2	16.0	14.8	13.5	~16%

The results indicate that vehicles with flat or nearly vertical front-end profiles tend to generate the largest pedestrian projection distances. This behavior is consistent with a forward projection mechanism, in which the pedestrian is pushed forward by the vehicle front rather than rotating over the hood in a classical wrap-around trajectory. In contrast, conventional passenger-car geometries, with a sloped hood and lower leading

edge, promote wrap-around kinematics, resulting in shorter projection distances and more pronounced body rotation over the vehicle front.

Overall, the results show that braking deceleration reduces pedestrian projection distance, but the dominant factor remains the vehicle front-end geometry. Flat and vertical profiles produce larger projection distances due to forward projection, whereas conventional sloped profiles generate shorter distances associated with wrap-around kinematics.

Many studies mention that vehicle braking influences pedestrian injury mechanisms through multiple coupled effects, which extend beyond a simple reduction of impact speed. While a lower impact velocity reduces the kinetic energy transferred during the vehicle–pedestrian contact, braking also significantly modifies pedestrian kinematics, including body rotation, trajectory, and post-impact motion. As a result, the pedestrian's subsequent interaction with the ground is altered, affecting both the timing and severity of the secondary impact. Previous studies have shown that braking can mitigate not only primary impact injuries but also those associated with ground contact. In particular, Rosén et al. [46], based on real-world accident data, demonstrated that pre-impact braking reduces impact energy and contributes to lowering the severity of secondary ground impacts. More recent work by Zou et al. [47] showed that controlled braking strategies can significantly reduce head impact velocity and overall injury metrics during the ground contact phase, emphasizing that braking effectiveness is strongly linked to pedestrian kinematics rather than impact speed alone. Further developments presented by Zou et al. [48] highlight that the combined effect of vehicle front-end geometry and controlled braking strategies can substantially alter the pedestrian ground impact mechanism. Their results indicate that braking not only reduces injury severity, but can also modify the pedestrian's trajectory such that the distance between the pedestrian and the vehicle at ground contact is reduced, potentially enabling additional protective interventions. At the same time, the study shows that different geometric configurations may lead to different kinematic responses, including variations in head impact timing and velocity, confirming that injury outcomes depend on both vehicle design and braking strategy. These findings reinforce the idea that pedestrian injury severity is governed not only by impact energy, but also by the dynamic evolution of the pedestrian during and after impact. Consequently, braking should be understood as a mechanism that reshapes the entire impact scenario, influencing both primary contact and secondary ground interaction.

Recent studies emphasize the importance of simulation-based environments for analyzing autonomous vehicle behavior under controlled and repeatable conditions. For example, Bakirci [49] developed a virtual simulation framework enabling consistent sensor-based data acquisition and reproducible testing scenarios. Although focused on vehicle maneuvering, such approaches highlight the broader relevance of virtual environments in studying vehicle–environment interactions. In the present work, the PC-Crash simulation framework fulfills a similar role, providing a controlled platform for analyzing pedestrian impact characteristics.

To quantitatively distinguish between wrap-around and non-rotational impact mechanisms, rotational dynamics indicators could be introduced in the future work. The angular momentum of the pedestrian body relative to its center of mass is defined as:

$$\mathrm{L} = I_{CM}\omega \tag{34}$$

where:

- I_{CM} is the moment of inertia about the center of mass,
- ω is the angular velocity.

The rotational kinetic energy is expressed as:

$$E_{rot} = \frac{1}{2} I_{CM} \omega^2 \tag{35}$$

while the translational kinetic energy is:

$$E_{trans} = \frac{1}{2} m v^2 \tag{36}$$

The ratio between rotational and translational energy, $\eta = \frac{E_{rot}}{E_{trans}}$ can be used as an indicator of impact mechanism. High values of η correspond to wrap-around kinematics, characterized by significant body rotation and head impact against the hood or windshield. Low values of η indicate forward projection, where rotation is suppressed and the body is primarily subjected to translational motion.

In the present simulations, conventional sloped front-end geometries promote higher angular momentum due to delayed torso contact, while vertical geometries generate early thoracic engagement, reducing rotational motion and increasing direct load transfer to the torso.

From an energy perspective, the total kinetic energy of the system is redistributed during impact into: translational motion, rotational motion, deformation energy, dissipated energy through contact and friction.

$$E_{total} = E_{trans} + E_{rot} + E_{def} + E_{diss} \tag{37}$$

where:

- E_{trans} translational kinetic energy;
- E_{rot} rotational kinetic energy,
- E_{def} deformation energy,
- E_{diss} dissipated energy, corresponding to energy losses due to friction, damping, and other non-conservative effects during the collision.

The presented energy curves, Fig. 22, represent the evolution of the pedestrian multibody system energy during and after impact, including translational and rotational kinetic energy components, as well as energy dissipation associated with contact interactions, friction, and secondary ground impacts within the PC-Crash multibody framework. The diagrams indicate that the main vehicle–pedestrian energy transfer occurs during the initial contact phase, within approximately the first 0.15–0.20 s. After this interval, the curves reach a quasi-stationary plateau, corresponding to the airborne motion of the pedestrian after separation from the vehicle. The end of this energetic plateau is closely correlated with the first contact of the pedestrian with the ground, after which the rolling/sliding phase on the asphalt begins until complete rest. For the ROBO1 and ROBO1_low configurations, the plateau ends at approximately 0.55–0.65 s, consistent with the very early ground contact of the pedestrian, first contact at 0.53 and 0.59 s, respectively. Similar behavior is observed for VAN2, where the energy decrease starts around 0.6–0.65 s. ROBO2 exhibits an intermediate behavior, with the plateau ending near 0.80–0.90 s, consistent with the first ground contact at approximately 0.81 s. In contrast, conventional passenger vehicles such as SM, CC, and EC show significantly longer plateau regions. For these vehicles, the major energy decrease begins around 1.1–1.4 s, corresponding to the delayed pedestrian-ground contact caused by wrap-around kinematics over the hood and windshield. Similar delayed behavior is also observed for SSUV and VAN1, where the pedestrian first contacts the ground at approximately 0.95 s.

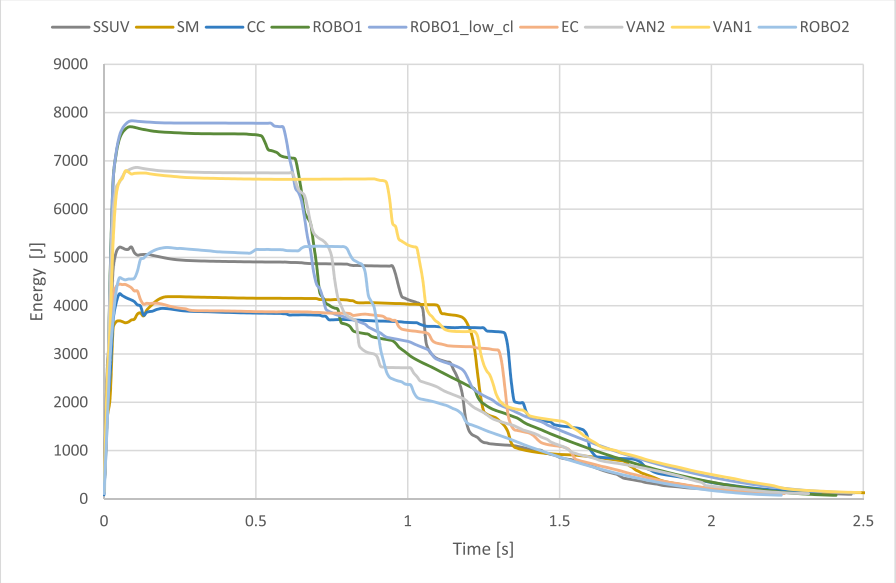

Figure 22: Pedestrian total energy during impact with vehicle.

Therefore, the duration of the energetic plateau reflects the pedestrian airborne phase after separation from the vehicle. Earlier plateau termination for vertical autonomous vehicle geometries indicates a faster projection toward the ground, while conventional sloped front-end vehicles generate longer airborne trajectories before the rolling/sliding phase on the road surface begins.

The energy level itself also varies significantly with vehicle front-end geometry. Vertical or nearly vertical autonomous vehicle configurations, such as ROBO1, ROBO1_low, VAN1, and VAN2, generate the highest energy levels, reaching approximately 6500–7800 J, indicating a more direct and concentrated transfer of impact energy to the pedestrian body. In contrast, conventional passenger vehicles such as SM, CC, and EC exhibit lower energy levels, typically around 3700–4500 J, reflecting a more progressive energy transfer associated with wrap-around pedestrian kinematics. Intermediate behavior is observed for SSUV and ROBO2 configurations, the latter combining characteristics specific to both vertical and sloped front-end geometries.

The results confirm that each collision scenario exhibits distinct energetic and kinematic behavior. Therefore, pedestrian injury severity cannot be directly generalized from pedestrian throw distance alone, since the same projection distance may result from substantially different impact mechanisms, force distributions, and secondary ground-contact conditions.

Vehicle geometry influences the partitioning of energy between these components. Sloped front-end geometries promote energy transfer into rotational motion, increasing head impact risk, while vertical geometries favor direct energy transfer into thoracic compression, increasing torso loading.

The present study is subject to several limitations. The simulations were conducted for a single standardized impact scenario, without explicit modeling of braking dynamics, vehicle pitch motion, or variations in pedestrian posture and orientation.

Furthermore, the use of a multibody pedestrian model enables efficient simulation of global kinematics but does not capture tissue-level deformation or internal injury mechanisms.

These assumptions were adopted to ensure a controlled comparison between vehicle geometries. Future work will extend the analysis to include variable impact conditions, advanced human body models, and more detailed structural representations.

Another limitation of the research, this study employed a validated multibody pedestrian model, which provides computational efficiency and scalability but does not capture tissue-level deformation or detailed organ response. Furthermore, thoracic injury risk was inferred from peak force metrics rather than detailed chest deflection or organ-level injury predictors. Future studies using finite element human body models may provide more detailed insight into thoracic injury mechanisms.

The multibody pedestrian model and contact formulations employed in this study have been previously validated against experimental data and accident reconstruction cases. However, empirical validation for emerging autonomous vehicle geometries, such as flat-front configurations (e.g., ROBO1), remains limited due to the lack of standardized test datasets.

Consequently, the current analysis should be regarded as a physics-based exploratory investigation, in which novel vehicle architectures are represented through parameterized extensions of validated models.

While the simulations are conducted under controlled impact conditions, real-world autonomous driving environments, particularly unstructured urban scenarios, are characterized by highly variable and unpredictable pedestrian behavior.

Due to the rigid-body nature of the multibody model, internal deformation-based injury criteria (e.g., chest deflection, viscous criterion) cannot be directly obtained. Such metrics typically require finite element human body models. According to standard crash analysis frameworks, thoracic injury criteria are often defined based on deformation or deformation rate rather than force alone. Therefore, thoracic peak force is used in this study as a comparative indicator of loading severity rather than a direct injury predictor.

Also, in the PC-Crash framework, the vehicle is modeled as a rigid body without explicit structural deformation or component-wise stiffness differentiation; consequently, contact interactions are governed by a global stiffness-based formulation, and the influence of vehicle design on pedestrian injury mechanisms arises primarily from geometric factors, such as contact point location, contact normal orientation, and impact sequence, rather than from local structural compliance, thereby enabling a consistent isolation of geometry-driven effects on load transfer and injury distribution.

7 Future Developments and Implications for Regulatory and Design Frameworks

Future research should extend the present findings through higher-fidelity human body models, including finite element simulations capable of capturing rib deflection, organ injury, and soft-tissue response, particularly for high thoracic loading observed in vertical autonomous configurations. Experimental validation using pedestrian impact tests or physical surrogate models is necessary to corroborate the simulated force magnitudes. Future autonomous vehicle design must therefore address not only geometric optimization but also stiffness distribution and sensor integration to mitigate localized injury risk.

Future work should therefore incorporate a broader range of conditions, including varying impact angles, pedestrian postures, and dynamic vehicle responses, to enable a more comprehensive evaluation of pedestrian injury mechanisms under realistic scenarios.

Without adaptation of assessment protocols, emerging vehicle designs may exhibit favorable head injury performance while posing increased thoracic and lower limb injury risk.

Sensor integration, vertical front symmetry, and potential wheel-first contact scenarios introduce new passive safety challenges that are not fully addressed by current pedestrian assessment protocols.

Future regulatory frameworks should consider both geometric optimization and localized stiffness management in autonomous vehicle platforms.

8 Conclusions

The results of this study suggest that existing pedestrian safety evaluation procedures, which often prioritize HIC thresholds, may be insufficient for emerging autonomous vehicle geometries. Van-type and symmetric flat-front designs can achieve low HIC values while simultaneously generating elevated thoracic loads.

This finding indicates the necessity of:

1. Balanced assessment of head and thorax injury criteria.
2. Explicit consideration of front-end verticality in safety standards.
3. Development of new test configurations for wheel-first or torso-dominant impacts.
4. Integration of geometric optimization guidelines into early-stage autonomous vehicle design.

Emerging vehicle platforms offer both opportunities and risks. While their electric architecture enables improved hood compliance and lower head injury metrics, flat and vertical front profiles may shift injury mechanisms toward potentially severe thoracic trauma. Simulation results demonstrate that these vehicles front-end geometry significantly redistributes pedestrian injury mechanisms. Conventional passenger car profiles produce higher head injury criteria, while flat or vertically oriented VAN/ROBO1-type geometries substantially reduce HIC values. However, this reduction in head injury risk is accompanied by a marked increase in thoracic and lower limb loading. Therefore, pedestrian protection in autonomous vehicles requires balanced optimization of both head and thorax injury criteria rather than focusing exclusively on HIC reduction.

Flat and vertical designs reduce wrap-around motion and lower HIC values but significantly increase thoracic loading due to direct torso engagement. Consequently, pedestrian safety optimization in autonomous vehicle must move beyond single-criterion evaluation and adopt a holistic, geometry-aware, multi-injury framework.

Acknowledgement: The authors would like to thank Transilvania University of Brasov for providing the necessary facilities and resources for conducting this research.

Funding Statement: The authors received no specific funding for this study.

Author Contributions: The authors confirm their contribution to the paper as follows: study conception and design: Adrian Soica, Bogdan Cornel Benea; data collection: Adrian Soica, Bogdan Cornel Benea; analysis and interpretation of results: Adrian Soica, Bogdan Cornel Benea; draft manuscript preparation: Adrian Soica, Bogdan Cornel Benea. All authors reviewed and approved the final version of the manuscript.

Availability of Data and Materials: The datasets generated during and/or analyzed during the current study are available from the corresponding author on reasonable request.

Ethics Approval: Not applicable.

Conflicts of Interest: The authors declare no conflicts of interest.

References

1. 2023 pedestrians traffic safety facts. [cited 2026 Jan 5]. Available from: https://Crashstats.Nhtsa.Dot.Gov/Api/Public/ViewPublication/813727.
2. World Health Organization. Pedestrian safety: a road safety manual for decision-makers and practitioners. Geneva, Switzerland: World Health Organization; 2013.
3. Kosgey G. The role of autonomous vehicles in urban mobility solutions. J Technol Syst. 2024;6(4):39–51. doi:10.47941/jts.2142.
4. Makahleh HY, Ferranti EJS, Dissanayake D. Assessing the role of autonomous vehicles in urban areas: a systematic review of literature. Future Transp. 2024;4(2):321–48. doi:10.3390/futuretransp4020017.
5. Hafiz D, AlKhafagy M, Zohdy I. Autonomous public transport: evolution, benefits, and challenges in the future of urban mobility. World Electr Veh J. 2025;16(9):482. doi:10.3390/wevj16090482.
6. Verstraete T, Muhammad N. Pedestrian collision avoidance in autonomous vehicles: a review. Computers. 2024;13(3):78. doi:10.3390/computers13030078.
7. Raul avelar speed. [cited 2025 Dec 30]. Available from: https://www.iihs.org/research-areas/speed.
8. Andrew J. Hawkins Waymo is still good at avoiding serious distraction and death after 56.7 million miles. [cited 2025 Dec 30]. Available from: https://www.theverge.com/news/658952/waymo-injury-prevention-human-benchmark-study.
9. Detwiller M, Gabler HC. Potential reduction in pedestrian collisions with an autonomous vehicle. In: Proceedings of the 25th International Technical Conference on the Enhanced Safety of Vehicles (ESV); 2017 Jun 5–8; Detroit, MI, USA.
10. Lee YK, Rhee YE, Ryu JK, Hahn S. Gentlemen on the road: understanding how pedestrians interpret yielding behavior of autonomous vehicles using machine learning. arXiv:2005.07872. 2020.
11. Deng X, Coxon S, Napper R. Designing for trust: enhancing passenger confidence in shared autonomous vehicles. Appl Sci. 2025;15(14):7765. doi:10.3390/app15147765.
12. Chidester AB, Isenberg RA. Final report-the pedestrian crash data study. In: Proceedings of the 17th International Technical Conference on the Enhanced Safety of Vehicles; 2001 Jun 4–7; Amsterdam, The Netherlands.
13. Longhitano D, Henaray B, Bhalla K, Ivarsson J, Crandall J. Influence of vehicle body type on pedestrian injury distribution. In: SAE technical paper 2005-01-1876. Washington, DC, USA: SAE; 2005. doi:10.4271/2005-01-1876.
14. Ballesteros MF, Dischinger PC, Langenberg P. Pedestrian injuries and vehicle type in Maryland, 1995–1999. Accid Anal Prev. 2004;36(1):73–81. doi:10.1016/S0001-4575(02)00129-X.
15. Gupta V, Yang KH. Effect of vehicle front end profiles leading to pedestrian secondary head impact to ground. Stapp Car Crash J. 2013;57:139–55. doi:10.4271/2013-22-0005.
16. Hamacher M, Eckstein L, Paas R. Vehicle related influence of post-car impact pedestrian kinematics on secondary impact. In: Proceedings of the 2012 IRCOBI Conference; 2012 Sep 12–14; Dublin, Ireland. p. 717–29.
17. Benea B, Soica A. The contact phase in vehicle–pedestrian accident reconstruction. Appl Sci. 2023;13(16):9404. doi:10.3390/app13169404.
18. Ahlgrimm J, Burg H, Dettinger J, Moser A. A10 fußgängerunfälle. In: Burg H, Moser A, editors. Handbuch verkehrsunfallrekonstruktion. Wiesbaden, Germany: Springer Fachmedien Wiesbaden; 2017. p. 395–430.
19. Moser A, Hoschopf H, Steffan H, Kasanicky G. Validation of the PC-crash pedestrian model. In: SAE 2000 World Congress; 2000 Mar 6; Detroit, MI, USA. doi:10.4271/2000-01-0847.
20. Fatzinger E, Landerville J, Tovar J, Nguyen B. Validation of a PC-crash multibody sport bike motorcycle model. SAE Int J Adv Curr Prac Mobility. 2021;3(4):1682–914. doi:10.4271/2021-01-0893.
21. Martínez F, Páez J, Furones A, Sánchez S. Pedestrian-vehicle accidents reconstruction with PC-crash®: sensibility analysis of factors variation. Transp Res Procedia. 2016;18:115–21. doi:10.1016/j.trpro.2016.12.016.
22. Mačužić Saveljić S, Miloradović D, Lukić N. Simulation of pedestrian throw distance in the software package pc-crash—comparison with experiment and theory. Mobil Veh Mech. 2023;49(3):65–75. doi:10.24874/mvm.2023.49.03.05.
23. Wdowicz D, Ptak M. Numerical approaches to pedestrian impact simulation with human body models: a review. Arch Computat Methods Eng. 2023;30(8):4687–709. doi:10.1007/s11831-023-09949-2.

24. Rose N, Smith C, Carter N, Metanias A. Validation of pedestrian collision reconstruction using the pc-crash multibody pedestrian model. In: Proceedings of the WCXTM™ 2025; 2025 Apr 1; Detroit, MI, USA. p. 1–25.
25. Crocetta G, Piantini S, Pierini M, Simms C. The influence of vehicle front-end design on pedestrian ground impact. Accid Anal Prev. 2015;79(1):56–69. doi:10.1016/j.aap.2015.03.009.
26. Niederer PF, Schlumpf MR. Influence of vehicle front geometry on impacted pedestrian kinematics. In: Proceedings of the 28th Stapp Car Crash Conference; 1984 Oct 1; Chicago, IL, USA. 841663 p.
27. Hu W, Monfort SS, Cicchino JB. The association between passenger-vehicle front-end profiles and pedestrian injury severity in motor vehicle crashes. J Saf Res. 2024;90(1):115–27. doi:10.1016/j.jsr.2024.06.007.
28. Monfort SS, Hu W, Mueller BC. Vehicle front-end geometry and in-depth pedestrian injury outcomes. Traffic Inj Prev. 2024;25(4):631–9. doi:10.1080/15389588.2024.2332513.
29. Soica A, Ispas N. The influence of the vehicle's front-end profile upon adult pedestrian kinematics and dynamics, multibody approach. Int J Veh Saf. 2012;6(2):134. doi:10.1504/IJVS.2012.049019.
30. Jonsén P, Isaksson E, Sundin KG, Oldenburg M. Identification of lumped parameter automotive crash models for bumper system development. Int J Crashworthiness. 2009;14(6):533–41. doi:10.1080/13588260902837262.
31. Ojalvo IU, Weber BE, Evensen DA, Szabo TJ, Welcher JB. Low speed car impacts with different bumper systems: correlation of analytical model with tests. In: Proceedings of the International Congress & Exposition; 1998 Feb 23; Detroit, MI, USA.
32. Dettinger J. Beitrag zur Verfeinerung der Rekonstruktion von Fußgängerunfällen—Abwicklungsdifferenz—Anstoßfaktor—Längswurfweiten von Fußgängern—Lage von Glassplittern. Verkehrsunfall Fahrzeugtechnik. 1996;34–35:324–30+25–30.
33. It's not a car. It's a robotaxi designed around you. [cited 2025 Dec 30]. Available from: https://zoox.com/.
34. PC-CRASH A. Simulation program for vehicle accidents, operating and technical manual, version 15.1. Linz, Austria: Dr. Steffan Datentechnik; 2025.
35. Spit HH. Evaluation of PC crash: as tool for professional traffic accident research and reconstruction. Eindhoven, The Netherlands: Technische Universiteit Eindhoven; 2000. 57 p.
36. Kolla E, Kolla PKE, Kohút P. Virtual human body model for PC-crash. Edinburgh, UK: EVU Conference; 2015. 24 p.
37. Ravani B, Brougham D, Mason RT. Pedestrian post-impact kinematics and injury patterns. In: Proceedings of the 25th Stapp Car Crash Conference; 1981 Oct 1; San Francisco, CA, USA.
38. Bastien C, Orlowski M, Bhagwani M. Validation of a finite element human model throw distance in pedestrian accident scenarios. In: Proceedings of the 11th European LS-DYNA Conference; 2017 May 9–11; Salzburg, Austria.
39. Crash analysis criteria description. [cited 2026 May 1]. Available from: http://crash-meeting.com/CrashAnalysisCriteria_2.1.1.pdf.
40. Soica A, Tarulescu S. Impact phase in frontal vehicle-pedestrian collisions. Int J Automot Technol. 2016;17(3):387–97. doi:10.1007/s12239-016-0040-y.
41. Sokolovskij E, Prentkovskis O. Investigating traffic accidents: the interaction between a motor vehicle and a pedestrian. Transport. 2013;28(3):302–12. doi:10.3846/16484142.2013.831771.
42. Fathi H, El-Sayegh Z, Ren J, El-Gindy M. Modeling and validation of a passenger car tire using finite element analysis. Vehicles. 2024;6(1):384–402. doi:10.3390/vehicles6010016.
43. Mhaske MP. Ahmednagar PC Analysis of vertical stiffness of passenger car tire at different pressure using Fe model. Int J Innov Eng Res Technol. 2021:1–6. [cited 2026 Jan 5]. Available from: https://repo.ijiert.org/index.php/ijiert/article/view/712.
44. Samaka H, Al-Bugharbee H, Al-Azawy M. Redesign the front shape of the Sedan car for pedestrian safety and mitigating leg injuries at accidents. Int J Saf Secur Eng. 2020;10(6):747–52. doi:10.18280/ijsse.100604.
45. Mark S. Pedestrian safety upper legform bumper impact simulation. In: Proceedings of the International Technical Conference on Enhanced Safety of Vehicles; 2001 Jun 4–7; Amsterdam, The Netherlands.
46. Rosén E, Källhammer JE, Eriksson D, Nentwich M, Fredriksson R, Smith K. Pedestrian injury mitigation by autonomous braking. Accid Anal Prev. 2010;42(6):1949–57. doi:10.1016/j.aap.2010.05.018.

47. Zou T, Shang S, Simms C. Potential benefits of controlled vehicle braking to reduce pedestrian ground contact injuries. Accid Anal Prev. 2019;129(2):94–107. doi:10.1016/j.aap.2019.05.008.
48. Zou T, Chen D, Zeng C, Ciaran S. The effectiveness of proposed pedestrian-friendly vehicle front-end shapes and their corresponding controlled braking methods in protecting pedestrian ground contact injuries. Chin J Mech Eng. 2025;13(1):100001. doi:10.1016/j.cjme.2025.100001.
49. Bakirci M. Simulation of autonomous driving for a line-following robotic vehicle: determining the optimal manoeuvring mode. Elektronika Elektrotechnika. 2023;29(6):4–11. doi:10.5755/j02.eie.32364.